Constraints on the Martian lithosphere from gravity and topography data

V. Belleguic

Département de Géophysique Spatiale et Planétaire, UMR7096, Institut de Physique du Globe de Paris, Saint-Maur, France

Joint Planetary Interior Physics Research Group of the University Münster and DLR, Berlin, Germany

P. Lognonné and M. Wieczorek

Département de Géophysique Spatiale et Planétaire, UMR7096, Institut de Physique du Globe de Paris, Saint-Maur, France

[1] Localized spectral admittances of the large Martian volcanoes are modeled by assuming that surface and subsurface loads are elastically supported by the lithosphere. In order to model the case where the load density differs from that of the crust, a new method for calculating gravity anomalies and lithospheric deflections is developed. The modeled gravity anomalies depend upon the elastic thickness, crustal thickness, load density, and crustal density, and these parameters were exhaustively sampled in order to determine their effect on the misfit between the observed and modeled admittance function. We find that the densities of the Martian volcanoes are generally well constrained with values of 3200 ± 100 kg m^{-3}, which is considerably greater than those reported previously. These higher densities are consistent with those of the Martian basaltic meteorites, which are believed to originate from the Tharsis and Elysium volcanic provinces. The crustal density is constrained only beneath the Elysium rise to be 3270 ± 150 kg m^{-3}. If this value is representative of the northern lowlands, then Pratt compensation is likely responsible for the approximately 6-km elevation difference between the northern and southern hemispheres. The elastic thicknesses of the major Martian volcanoes (when subsurface loads are ignored) are found to be the following: Elysium rise (56 ± 20 km), Olympus Mons (93 ± 40 km), Alba Patera (66 ± 20 km), and Ascraeus Mons (105 ± 40 km). We have also investigated the effects of subsurface loads, allowing the bottom load to be located either in the crust as dense intrusive material or in the mantle as less dense material. We found that all volcanoes except Pavonis are better modeled with the presence of less dense material in the upper mantle, which is indicative of either a mantle plume or a depleted mantle composition. An active plume beneath the major volcanoes is consistent with recent analyses of cratering statistics on Olympus Mons and the Elysium rise, which indicate that some lava flows are as young as $10-30$ Myr, as well as with the crystallization ages of the Shergottites, of which some are as young as 180 Myr.

Citation: Belleguic, V., P. Lognonné, and M. Wieczorek (2005), Constraints on the Martian lithosphere from gravity and topography data, *J. Geophys. Res.*, *110*, E11005, doi:10.1029/2005JE002437.

1. Introduction

[2] Before seismometers are deployed on Mars [e.g., *Lognonné et al.*, 2000], gravity and topography measurements are the primary data sets from which the properties of a planet's crust and upper mantle can be constrained. A common approach is to consider that, over geological time, the lithosphere behaves as an elastic plate overlaying a fluid mantle and to model the lithospheric deformations produced by topographic and/or internal density anomalies [e.g., *Turcotte et al.*, 1981; *Forsyth*, 1985]. The resulting gravity anomalies depend upon physical parameters such as the densities of the crust and load, and the thicknesses of the elastic lithosphere and crust.

[3] To date, only a few localized admittance studies have been applied to Mars using recent Mars Global Surveyor (MGS) data. Using line of sight gravitational acceleration profiles, *McKenzie et al.* [2002] inverted for the crustal density and elastic thickness at various locales by modeling the one-dimensional Cartesian gravitational admittance function. Only surface loads were considered in that study, but this assumption was never justified by comparing the observed and modeled coherence functions. It was further assumed that the load density was the same as the crustal density, which is unlikely to be true for the Martian

volcanoes [e.g., *Neumann et al.*, 2004]. Using a similar approach, *Nimmo* [2002] modeled the mean crustal thickness, the elastic thickness and the surface density for a region centered on the hemispheric dichotomy. The theoretical admittance model utilized in his study assumed that surface and subsurface loads were uncorrelated, but this hypothesis was not tested by comparing the observed coherence function with the predicted one. Moreover, as emphasized by *Pérez-Gussinyé et al.* [2004], the results of these two studies could be biased as the employed multi-taper spectral estimation procedure was not consistently applied to both the data and theoretical model. Finally, *McGovern et al.* [2002] calculated admittance and coherence spectra for several volcanic regions employing the spatiospectral localization method of *Simons et al.* [1997]. Their lithospheric flexure model took into account both surface and subsurface loads (assumed to be in phase) and a load density that differed from that of the crust. While the elastic thickness and load density were constrained for certain regions, several factors have led us to reconsider their results. In particular, the degree-1 surface topography was treated as a load in their study, and the surface load was not calculated in a self-consistent manner when the load density differed from the crustal density. We have further found that the modeled and observed admittances were mistakenly calculated at two different radii causing their modeled densities to be underestimated by approximately 300 kg m^{-3} [see *McGovern et al.*, 2004].

[4] In the above-mentioned studies, and in previous global ones such as *Banerdt* [1986] and *Turcotte et al.* [1981], various approximations have been made in order to calculate quickly the lithospheric deflection and the predicted gravity field. However, some of these assumptions may not be entirely applicable to Mars as it is a small planet with extreme topographic variations. As an example, the use of the "mass-sheet" approximation when computing the gravity anomaly of a large volcano on Mars can introduce an error of up to 500 mgals, corresponding to ~25% of the signal [*McGovern et al.*, 2002]. In addition, the magnitude of this lithospheric load depends upon the local gravitational potential within the crust, and this is a function of the lithospheric deflection. While a computationally efficient method that considers finite amplitude relief in the calculation of gravity anomalies exists in the spherical domain [*Wieczorek and Phillips*, 1998], this method is only applicable on a sphere whose radius is either greater than the maximum elevation of the planet or smaller than the minimum depth of lateral density variations. Hence this method cannot be used to calculate exactly the potential at arbitrary points within a planet, nor the load acting on the lithosphere.

[5] In order to improve the accuracy of the theoretical flexure and admittance models, we have here developed a new numerical method that precisely calculates both the load acting on the lithosphere due to an arbitrary density distribution and the corresponding lithospheric deflection that is affordable from a computational point of view. As recent studies have highlighted the evidence for recent volcanic activity on Mars [*Nyquist et al.*, 2001; *Hartmann and Neukum*, 2001; *Neukum et al.*, 2004], the Martian mantle must be still active, and variations in either temperature or composition are likely to play an important role in

the observed gravity and topography fields. We have therefore investigated the effects of subsurface loads acting on the lithosphere, either as dense intrusive materials in the crust or buoyant materials in the mantle. This latter possibility could be a result of temperature anomalies in a mantle plume and/or a depleted mantle composition.

[6] We have generated surface and subsurface loading models by exhaustively sampling all possible values (within limits) of the load density, the crustal density, the elastic and crustal thicknesses, and the ratio of surface to subsurface loads. The misfit between the observed and modeled admittance and correlation functions of the gravity and topography fields, localized to the major Martian volcanoes, was then quantified. In this study, we use the spectral localization procedure developed by *Wieczorek and Simons* [2005] and use localizing windows that concentrate ~99% of their energy within the region of interest. This is in comparison to the windows employed by *McGovern et al.* [2002] (developed by *Simons et al.* [1997]), which are only concentrated at ~90%.

2. Method

[7] The lithospheric model used here is shown in Figure 1. It consists of a surface load, such as a volcano, with a density ρ_l supported by a thin elastic lithosphere of thickness T_e overlying a weak mantle that behaves as a fluid over geological time. The load deforms the lithosphere with a displacement w (measured positive downward) which is presumed to be the same for each density interface. This deflection depends on several parameters, and the following are investigated in this study: the load density ρ_l, the crustal density ρ_c, the crustal thickness T_c, the elastic thickness T_e, and subsurface loads. The model is subdivided by five major density interfaces (see Table 1): (1) R_0, a spherical interface exterior to the planet of mean planetary radius R, (2) the surface, $R + h$, (3) the base of the crust, $R - T_c - w$, (4) the base of the lithosphere, $R - T_e - w$ and (5) a spherical interface within the non-lithospheric part of the mantle, $R - T_c - M$.

[8] In this section we describe the method developed for calculating the gravity field associated with this lithospheric deformation. The major improvement over previous studies is a more rigorous methodology for computing both the gravity anomaly and the magnitude of the load acting on the lithosphere when the load density differs from that of the crust.

2.1. Modeling the Gravity Anomaly

[9] Our method allows for the calculation of the gravitational potential both inside and outside of an aspherical and laterally heterogeneous planet. All calculations are performed on a grid in the space domain where the grid spacing was chosen to facilitate spherical harmonic transforms and their corresponding spatial reconstructions. For an arbitrary density distribution, we need to solve the gravitational differential equations

$$\mathbf{G} = \nabla U , \qquad (1)$$

$$\nabla \cdot \mathbf{G} = -4\pi \mathcal{G} \rho, \qquad (2)$$
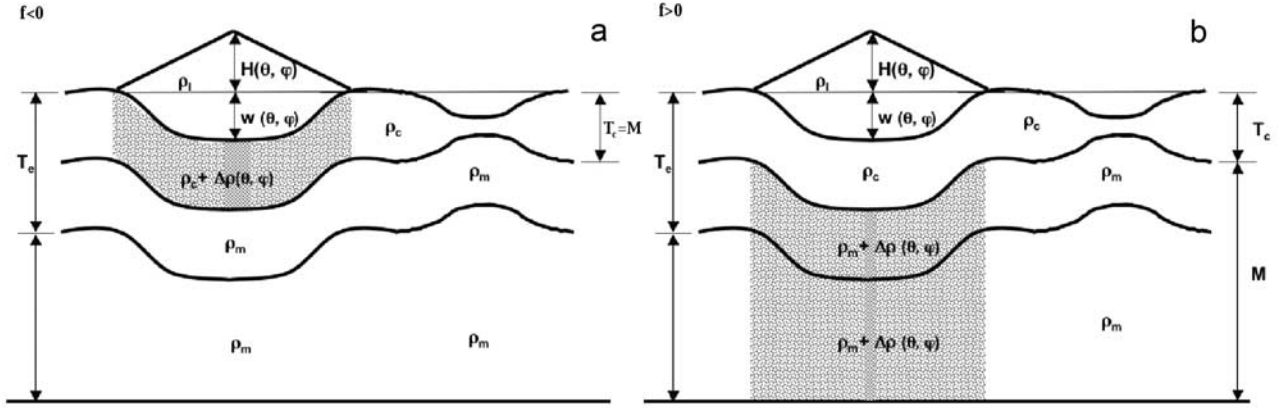
Figure 1. Schematic representation of the lithospheric loading model. $h(\theta,\phi)$ is the surface topography and $w(\theta,\phi)$ is the flexural deformation, both measured with respect to the mean planetary radius. T_c, T_e, and M are the crustal thickness, the elastic thickness, and the thickness of the subsurface load, respectively. ρ_l, ρ_c, and ρ_m are the densities of the surface load, the crust, and the mantle, respectively, and $\Delta\rho$ is the lateral density anomaly associated with the subsurface loads. Two cases of buried loads are represented: (a) one where the subsurface load is located in the crust, with $M = T_c$, and (b) the other where the subsurface load is present in the mantle to a depth M beneath the crust.

both within and exterior to the planet, where **G** is the gravity vector (assumed to be positive upward), U is the gravitational potential, ρ the density and $\mathcal{G}$ the gravitational constant. **G**, U and ρ implicitly depend on the spherical coordinates r, θ and ϕ. This set of first-order differential equations can be solved numerically if the interior density structure of the planet is known. We first compute exactly **G** and U, as well as their first derivatives, at a radius R_0 exterior to the planet using a generalization of the method described by *Wieczorek and Phillips* [1998], here modified to allow for lateral variations of density (see Appendix B for details). Using the first radial derivatives of U and **G**, these fields can be estimated at a different radius using a first order Taylor series. By repeating this procedure, we can estimate the potential and gravity field anywhere inside or outside a planet.

[10] To avoid numerical errors and to simplify the calculations, a set of curvilinear coordinates (s, θ, ϕ) is used that reduces irregular interfaces to spherical ones. The relationship between the two sets of coordinates between r_i and r_{i+1} is given by

$$r(s,\theta,\phi) = r_i(\theta,\phi) + [r_{i+1}(\theta,\phi) - r_i(\theta,\phi)]\frac{s - S_i}{S_{i+1} - S_i}, \quad (3)$$

where S_i defines the mean radius of the ith density interface with associated relief $r_i(\theta, \phi)$. In practice, s takes discrete values between S_i and S_{i+1}, and these values will be denoted by s_j. We next transform equations (1) and (2) to this new set of coordinates and obtain expressions for the partial derivatives of U and **G** with respect to s. Here we only quote the relevant results, and refer the reader to Appendix A for further details. Between $r(S_i, \theta, \phi)$ and $r(S_{i+1}, \theta, \phi)$ equation (1) reduces to two equations:

$$\frac{\partial U}{\partial s} = C_1\, G_r, \quad (4)$$

Table 1. Summary of the Interfaces and Densities Used in the Gravity Field Computations

Medium	Topographic Interfaces	Spherical Interfaces	Densities
Vacuum	$r_5(\theta,\phi) = R_0$ $r_4(\theta,\phi) = R + h(\theta,\phi)$	$S_5 = R_0$ $S_4 = R$	$\rho_0 = 0$ kg m^{-3}
Crust	$r_4(\theta,\phi) = R + h(\theta,\phi)$ $r_3(\theta,\phi) = R - T_c - w(\theta,\phi)$	$S_4 = R$ $S_3 = R - T_c$	$\rho_0 = \begin{cases} \rho_l & \text{if } r \geq R - w(\theta,\phi) \\ \rho_c & \text{otherwise} \end{cases}$ $\Delta\rho(\theta,\phi) = -\frac{\rho_l h_l}{M}f$ if $r_3(\theta,\phi) \leq r \leq R - w(\theta,\phi)$ and $f < 0$
Lithospheric mantle	$r_3(\theta,\phi) = R - T_c - w(\theta,\phi)$ $r_2(\theta,\phi) = R - T_e - w(\theta,\phi)$	$S_3 = R - T_c$ $S_2 = R - T_e$	$\rho_0 = \rho_m$ $\Delta\rho(\theta,\phi) = \begin{cases} -\frac{\rho_l h_l}{M}f & \text{if } f > 0 \\ 0 & \text{if } f \leq 0. \end{cases}$
Mantle	$r_2(\theta,\phi) = R - T_e - w(\theta,\phi)$ $r_1(\theta,\phi) = R - T_c - M$	$S_2 = R - T_e$ $S_1 = R - T_c - M$	$\rho_0 = \rho_m$

and

$$\mathbf{G}_\Sigma = \nabla_{\Sigma_s} U - [C_2 \nabla_{\Sigma_s} r_{i+1} + C_3 \nabla_{\Sigma_s} r_i] \frac{\partial U}{\partial s}, \qquad (5)$$

where $\mathbf{G}_\Sigma$ is the horizontal gravity field and ∇_{Σ_s} is the horizontal gradient operator calculated along a surface of constant s. The parameters C_1, C_2 and C_3 (which depend upon θ and ϕ) are given by

$$C_1 = \frac{r_{i+1}(\theta, \phi) - r_i(\theta, \phi)}{S_{i+1} - S_i}, \qquad (6)$$

$$C_2 = \frac{s - S_i}{r_{i+1}(\theta, \phi) - r_i(\theta, \phi)}, \qquad (7)$$

$$C_3 = \frac{S_{i+1} - s}{r_{i+1}(\theta, \phi) - r_i(\theta, \phi)}. \qquad (8)$$

Equation (2) yields

$$\frac{\partial G_r}{\partial s} = -C_1 \left[4\pi \mathcal{G}\rho + \frac{2G_r}{r} + \frac{1}{r} \nabla_{\Sigma_s} \cdot \mathbf{G}_\Sigma \right]$$
$$+ C_1 [C_2 \nabla_{\Sigma_s} r_{i+1} + C_3 \nabla_{\Sigma_s} r_i] \cdot \frac{\partial \mathbf{G}_\Sigma}{\partial s}, \qquad (9)$$

where $\nabla_{\Sigma_s} \cdot \mathbf{G}_\Sigma$ is the horizontal divergence at constant s (see equation (A25)). In the above equations, r, G_r, $\mathbf{G}_\Sigma$, U, ρ, C_1, C_2 and C_3 are implicitly functions of the three mapped coordinates s, θ and ϕ.

[11] In order to determine the first derivative of G_r with respect to s, it is necessary to calculate the horizontal gravity field, $\mathbf{G}_\Sigma$, and its horizontal divergence. As both U and $\mathbf{G}$ are initially known on a set of grid points (θ_k, ϕ_k) of constant s, these calculations are most easily performed in the spectral domain after having expanded these fields in spherical harmonics. While the derivatives of U and the surface gradient of $\mathbf{G}$ could be performed using ordinary spherical harmonics, the obtained relationships are cumbersome. Instead, these calculations are greatly facilitated by using the generalized spherical harmonics, as described in detail by *Phinney and Burridge* [1973]. In this basis, the potential and three components of the gravity field can be expressed as (see Appendix C)

$$U(s, \theta, \phi) = \sum_{\ell=0}^{L} \sum_{m=-\ell}^{\ell} U_{\ell m}(s) Y_\ell^m(\theta, \phi), \qquad (10)$$

$$G^\alpha(s, \theta, \phi) = \sum_{\ell=0}^{L} \sum_{m=-\ell}^{\ell} G_{\ell m}^\alpha(s) Y_\ell^{\alpha m}(\theta, \phi), \qquad (11)$$

where L is the maximum degree of the expansion, $U_{\ell m}$ and $G_{\ell m}^\alpha$ are the complex coefficients corresponding to the generalized spherical harmonics $Y_\ell^{\alpha m}$, and α is defined to be either $-$ or $+$ for the two horizontal components, and 0 for the radial component. We note that in our case, where

the gravity field is real and has only a poloidal component, $G_{\ell m}^+ = G_{\ell m}^-$ [see *Phinney and Burridge*, 1973]. We further note that Y_ℓ^{0m} is equal to the standard complex spherical harmonic Y_ℓ^m. After expanding $U(s, \theta, \phi)$, $\mathbf{G}(s, \theta, \phi)$ and $r_i(\theta, \phi)$ in spherical harmonics, the horizontal derivatives of U and $r(\theta, \phi)$ can be calculated using equation (C11), and the horizontal divergence of $\mathbf{G}$ can be calculated using equation (C14). We note that equations (4)–(9) are valid for both the spherical and canonical basis. These spherical harmonic operations were performed using the software package of *Clévédé and Lognonné* [2003].

[12] Once $\partial U/\partial s$ and $\partial G_r/\partial s$ have been obtained at a given point (s, θ, ϕ), we estimate U and G_r at $s + \Delta s$ using a first order Taylor series (we note that since we perform a downward propagation, Δs is negative):

$$U(s + \Delta s, \theta, \phi) = U(s, \theta, \phi) + \Delta s \frac{dU(s, \theta, \phi)}{ds}, \qquad (12)$$

$$G_r(s + \Delta s, \theta, \phi) = G_r(s, \theta, \phi) + \Delta s \frac{dG(s, \theta, \phi)}{ds}. \qquad (13)$$

The error associated with this approximation decreases with decreasing Δs. On the basis of a comparison with a more robust Runge-Kutta integration technique, we have chosen to use 50 equally spaced layers exterior to the planet where the density is zero and 100 equally spaced layers within both the crust and the mantle lithosphere.

2.1.1. Resolution by a Perturbation Approach

[13] In order to reduce numerical errors, we have separated the gravity and potential fields into two components: a reference component that corresponds to a density model that is spherically symmetric in the mapped coordinates, and a "perturbed" component defined as the difference between the total and the reference fields. Note that the reference component is not equal to the degree 0 of the total field, except when s = r. For each value of s, we write these fields as

$$U(s, \theta, \phi) = U_0(s) + U_1(s, \theta, \phi), \qquad (14)$$

$$\mathbf{G}(s, \theta, \phi) = G_0(s) \mathbf{e}_r + G_1(s, \theta, \phi) \mathbf{e}_r + \mathbf{G}_\Sigma(s, \theta, \phi), \qquad (15)$$

where the subscripts 0 and 1 correspond to the reference and perturbed terms, respectively. Since the reference field is spherically symmetric, it has no horizontal components, and $\mathbf{G}_\Sigma$ is a first order term. For the reference components, $r = s$, and $G_0(s)$ and $U_0(s)$ are calculated analytically. Since the reference components are also solutions of equations (1) and (2), we obtain the following relations for their radial derivatives:

$$\frac{\partial U_0}{\partial s} = G_0, \qquad (16)$$

$$\frac{\partial G_0}{\partial s} = -4\pi \mathcal{G}\rho_0 - \frac{2G_0}{s}. \qquad (17)$$

Table 2. Parameter Values Used in the Flexure Model

Parameter	Symbol	Value	Increment	Unit
Mean planetary radius	R	3389.5	-	km
Young's modulus	E	10^{11}	-	Pa
Poisson's ratio	ν	0.25	-	-
Mantle density	ρ_m	3500	-	kg m^{-3}
Crustal density	ρ_c	2700–3400	100	kg m^{-3}
Load density	ρ_l	2700–3400	100	kg m^{-3}
Elastic thickness	T_e	0–200	5	km
Crustal thickness	T_c	30–90	10	km
Load ratio	f	−0.3–0.5		
Subsurface load thickness	M	250	-	km

After replacing U and G_r by $U_0 + U_1$ and $G_0 + G_1$, respectively, in equations (4)–(9), and using equations (16) and (17) to simplify the resulting relations, we obtain

$$\frac{\partial U_1}{\partial s} = C_1 \, G_1 + (C_1 - 1) \, G_0, \qquad (18)$$

$$
\begin{aligned}
\frac{\partial G_1}{\partial s} = &- C_1 \left[4\pi\mathcal{G}\delta\rho(s,\theta,\phi) + \frac{1}{r}\nabla_{\Sigma_s}\cdot\mathbf{G}_{\Sigma_s} + \frac{2G_1}{r} \right] \\
&+ C_1 [C_2 \nabla_{\Sigma_s} r_{i+1}(\theta,\phi) + C_3 \nabla_{\Sigma_s} r_i(\theta,\phi)] \cdot \frac{\partial \mathbf{G}_\Sigma}{\partial s} \\
&- 4\pi\mathcal{G}\rho_0 (C_1 - 1) \\
&+ \left[\frac{r_i(\theta,\phi)S_{i+1} - r_{i+1}(\theta,\phi)S_i}{S_{i+1} - S_i} \right] \frac{2G_0}{s\,r},
\end{aligned}
\qquad (19)
$$

where $\delta\rho(s,\theta,\phi) = \rho(s,\theta,\phi) - \rho_0(s)$ is the lateral variation in density. Equation (5) gives us the supplementary equation

$$
\mathbf{G}_\Sigma = \nabla_{\Sigma_s} U_1 - [C_2 \nabla_{\Sigma_s} r_{i+1}(\theta,\phi) + C_3 \nabla_{\Sigma_s} r_i(\theta,\phi)]\left(\frac{\partial U_1}{\partial s} + G_0 \right).
\qquad (20)
$$

As before, U_1, G_1 and G_Σ in the above equations implicitly depend upon s, θ and ϕ, and all partial derivatives are calculated at constant s.

2.1.2. A Recipe for Computing the Gravity Field

[14] For clarity, we here recall the main steps involved in computing the gravity field anywhere within or exterior to a body possessing an arbitrary density structure.

[15] 1. In order to initiate the propagation of the fields, we define the main characteristics of the model.

[16] (i) First, define a grid (θ_k, ϕ_k) on which U and $\mathbf{G}$ will be computed and propagated. While the propagations will be performed at each individual grid point, some operations such as the horizontal derivatives and the horizontal divergence are most easily performed in the spectral domain, and then reconstructed in the space domain. In order to facilitate the spherical harmonic transformations and reconstructions, it is convenient to use a grid that is equally spaced in the ϕ direction, and with points in the θ direction corresponding to the Gauss-Legendre quadrature nodes [see *Lognonné and Romanowicz*, 1990; *Driscoll and Healy*, 1994; *Sneeuw*, 1994]. The grid used here is 128 × 256.

[17] (ii) Next, define the major density interfaces. Our model uses five interfaces $r_i(\theta, \phi)$: a spherical interface

whose radius is greater than the maximum elevation of the planet, the surface, the base of the crust, the base of the lithosphere, and a spherical interface within the non-lithostatic portion of the mantle (see Table 1).

[18] (iii) When propagating the gravity and potential fields, a first order Taylor expansion is used. In order to minimize the errors associated with this approximation, we discretize s between the major interfaces S_i using a step length Δs (these are denoted by s_j, and Δs is negative as we propagate downward). In our case, we define 50 sublayers outside the planet, and 100 sublayers within both the crust and mantle, for a total number of $N = 250$ layers. The relief along each interface is mapped to the coordinates (s_j, θ_k, ϕ_k) by use of equation (3). The reference density $\rho_0(s)$ between each interface is set, and the lateral density variations $\Delta\rho(s_j, \theta_k, \phi_k)$ are defined (see Table 2).

[19] 2. Next, calculate the initial values of U_0, U_1, G_0 and G_1 on the spherical interface S_5 according to the following steps.

[20] (i) First, set s_j equal to $s_N = R_0$, which is the uppermost layer in the model.

[21] (ii) Using the density interfaces defined in step 1, compute $U(s_j, \theta_k, \phi_k)$ and $G_r(s_j, \theta_k, \phi_k)$ on the spherical interface R_0 exterior to the planet using the method described in Appendix B.

[22] (iii) Obtain $U_1(s_j, \theta_k, \phi_k)$ and $G_1(s_j, \theta_k, \phi_k)$ by subtracting the reference fields $U_0(R_0) = \mathcal{G}M/R_0$ and $G_0(R_0) = -\mathcal{G}M/R_0^2$ from U and G_r, where M is the mass of the planet.

[23] 3. In order to propagate U downward, we need to calculate the radial derivative $\partial U_1(s_j, \theta_k, \phi_k)/\partial s$. This is calculated according to the following steps.

[24] (i) For the layer s_j, determine the value of i such that $S_i < s_j \leq S_{i+1}$.

[25] (ii) Calculate G_0 analytically from $G_0(s_j) = -\mathcal{G}M(s_j)/s_j^2$, where $M(s_j)$ is the mass interior to radius s_j.

[26] (iii) Update the function C_1, which depends upon $r_i(\theta_k, \phi_k)$, $r_{i+1}(\theta_k, \phi_k)$, S_i and S_{i+1}.

[27] (iv) Using $G_1(s_j, \theta_k, \phi_k)$, $\partial U_1(s_j, \theta_k, \phi_k)/\partial s$ is computed from equation (18).

[28] 4. The tangential component of the gravity field is required when calculating the derivative $\partial G_1/\partial s(s_j, \theta_k, \phi_k)$. This is calculated from equation (20) according to the following steps.

[29] (i) Update the functions C_2 and C_3, which depend upon $r_i(\theta_k, \phi_k)$, $r_{i+1}(\theta_k, \phi_k)$, S_i, S_{i+1} and s_j. Note that C_2 is exactly zero when $s_j = S_i$, and that C_3 is exactly zero when $s_j = S_{i+1}$.

[30] (ii) Calculate the horizontal gradients of U_1 along a surface of constant s, $\nabla_{\Sigma_s} U_1(s_j, \theta_k, \phi_k)$. This is most easily performed by first expanding $U_1(s_j, \theta_k, \phi_k)$ in spherical harmonics, and then reconstructing equation (C11) in the space domain.

[31] (iii) In a similar manner, calculate the horizontal gradients of $r_i(\theta_k, \phi_k)$ and $r_{i+1}(\theta_k, \phi_k)$ along a surface of constant s. Note that these are exactly zero for a spherical interface, such as S_5.

[32] (iv) Using $\partial U_1/\partial s$ and G_0 from step 3, calculate $\mathbf{G}_\Sigma(s_j, \theta_k, \phi_k)$ using equation (20).

[33] 5. In order to propagate downward $G_1(s_j, \theta_k, \phi_k)$ and $\mathbf{G}_\Sigma(s_j, \theta_k, \phi_k)$, we need to calculate the radial derivatives of $G_1(s_j, \theta_k, \phi_k)$ and $\mathbf{G}_\Sigma(s_j, \theta_k, \phi_k)$. These are calculated according to the following steps.

[34] (i) $\partial \mathbf{G}_\Sigma / \partial s$ is estimated using a finite difference formula between two layers:

$$\frac{\partial \mathbf{G}_\Sigma(s_j, \theta, \phi)}{\partial s} = \frac{\mathbf{G}_\Sigma(s_j - \Delta s, \theta, \phi) - \mathbf{G}_\Sigma(s_j, \theta, \phi)}{-\Delta s}, \quad (21)$$

noting that Δs is negative since we are propagating downward. This derivative is not needed when propagating from the first spherical interface, as the factors which multiply this term in equation (19) are identically zero.

[35] (ii) The horizontal divergence along a surface of constant s, $\nabla_{\Sigma_s} \cdot \mathbf{G}_\Sigma$, is next calculated. This is most easily performed by expanding $\mathbf{G}_\Sigma(s_j, \theta_k, \phi_k)$ in generalized spherical harmonics (see equation (C8)), and with the obtained coefficients $G_{\ell m}^+$ and $G_{\ell m}^-$, the divergence is calculated using equation (C14). We note that $G_{\ell m}^+ = G_{\ell m}^-$ for gravitational fields, which are both real and poloidal.

[36] (iii) At this point, all the necessary terms in equation (19) have been calculated in order to determine $\partial G_1 / \partial s(s_j, \theta_k, \phi_k)$.

[37] 6. Using $U_1(s_j, \theta_k, \phi_k)$, $G_1(s_j, \theta_k, \phi_k)$ and the above calculated partial radial derivatives, $U_1(s_j + \Delta s, \theta_k, \phi_k)$ and $G_1(s_j + \Delta s, \theta_k, \phi_k)$ are obtained using the first order expressions of equations (12) and (13).

[38] 7. Set $s_j = s_j + \Delta s$, and continue at step 3.

2.2. Modeling the Lithospheric Deflection

[39] Assuming that the rheology of planetary bodies can be approximated by that of an elastic lithosphere overlying a fluid mantle, the relationship that links the pressure acting on the shell p to the vertical displacement w is [Kraus, 1967; Turcotte et al., 1981]

$$D\nabla^6 w + 4D\nabla^4 w + ET_e R^2 \nabla^2 w + 2ET_e R^2 w = R^4(\nabla^2 + 1 - \nu)p, \quad (22)$$

where $D = ET_e^3/12(1 - \nu^2)$ is the flexural rigidity, E is Young's modulus, ν is Poisson's ratio, T_e is the elastic thickness and R is the radius of the shell, here taken to be the mean planetary radius. The pressure p (positive directed inward) and the displacement w (measured positive downward) depend upon position θ and ϕ. (We note that Turcotte et al. [1981] omitted a term $4D\nabla^2 w$ in equation (22) [Willemann and Turcotte, 1981], but that this term is in practice negligible.) In this equation, it is implicitly assumed that the thickness of the lithosphere is the same everywhere and small with respect to the planetary radius [cf. Zhong and Zuber, 2000]. Given that the expected elastic thicknesses are much smaller than a tenth of the planetary radius, this thin shell approximation should not give rise to any appreciable errors. Additionally, horizontal forces caused by topography along density interfaces are neglected, as in most previous studies [e.g., Kraus, 1967; Turcotte et al., 1981; McGovern et al., 2002], since they only have a small influence on the vertical displacement [see Banerdt, 1986].

[40] The net load p on the lithosphere is the difference between the gravitational force per unit area acting on the lithosphere, q_a, and the hydrostatic pressure within the fluid mantle q_h at the base of the lithosphere:

$$p(\theta, \phi) = q_a(\theta, \phi) - q_h(\theta, \phi). \quad (23)$$

We note that given the sign convention of p, q_a is defined positive downward and q_h positive upward. In previous studies, this load has been expressed in a first order form in order to obtain a linear relation between the surface topography h, and the lithospheric deflection w. For example, Turcotte et al. [1981] employed a mass-sheet approximation when calculating the gravity field and assumed that the geoid and gravitational acceleration did not vary with depth in the elastic shell, giving rise to the equation

$$p = g[\rho_c h - \rho_m h_g - (\rho_m - \rho_c)w],$$

where ρ_c and ρ_m are the density of the crust and mantle, respectively, h_g is the geoid (i.e., the height to an equipotential surface) and g is the mean amplitude of the gravitational acceleration at the surface. Other methods have been employed which yield similar linear relationship between p and w. In Banerdt [1986], the geoid was not assumed to be constant at all depths in the lithosphere, and both the geoid at the surface and at the base of the crust-mantle interface (i.e., the Martian "Moho") appear in the expression of p (see Appendix D). In McGovern et al. [2002], p is defined in a similar manner to Banerdt [1986] except that the topography was referenced to the observed geoid and the geoid was assumed to be zero at the base of the crust. In this latter study, the load density, ρ_l, was allowed to differ from the crustal density, but as we show in section 3.1 and Appendix D, the equations that were used are not entirely self consistent.

[41] In this section, we describe a self consistent method by which the lithospheric load p and the corresponding deflection w are determined exactly within the framework of a thin elastic spherical shell formulation. We will see that the load p depends upon the value of U inside the planetary body, which is easily calculated using our method described in section 2.1.

2.2.1. Gravitational Force Acting on the Lithosphere

[42] The vertical gravitational force acting downward on an infinitesimal volume of lithosphere centered at θ, ϕ is

$$F = -d\Omega \int_{r_2}^{r_4} G_r(r, \theta, \phi)\rho(r, \theta, \phi)r^2 dr, \quad (24)$$

where $r_2(\theta, \phi) = R - T_e - w(\theta, \phi)$ is the base of the lithosphere and $r_4(\theta, \phi) = R + h(\theta, \phi)$ is the surface, as defined in Table 1; G_r is the vertical component of the gravity field (defined positive upward), R is the mean planetary radius, and $d\Omega$ is the differential solid angle of the surface element. The gravitational force per unit surface area is then given by

$$q_a = \frac{F}{d\Omega R^2}. \quad (25)$$

Since $G_r = \partial U / \partial r$, equation (25) can be written as

$$q_a = -\frac{1}{R^2} \int_{U(r_2)}^{U(r_4)} \rho(r, \theta, \phi)r^2 dU, \quad (26)$$

and we approximate the integral numerically by the approximation

$$q_a = -\frac{1}{R^2} \sum_{j=1}^{N_L} \rho(r_j) r_j^2 [U(r_{j+1}) - U(r_j)], \quad (27)$$

where N_L is the number of layers in the lithosphere, $j = 1$ corresponds to the base of the lithosphere, r_j refers to $r(s_j)$, and $\rho(r_j)$, r_j, $U(r_j)$ and $U(r_{j+1})$ implicitly depend upon θ and ϕ.

2.2.2. Hydrostatic Pressure Acting on the Lithosphere

[43] The equation for hydrostatic equilibrium is

$$\frac{dq_h}{dr} = \rho(r)G_r(r, \theta, \phi) = \rho(r)\frac{dU(r, \theta, \phi)}{dr},$$

where we have assumed that the density of the fluid mantle is constant. Integrating this equation yields

$$\int_{R-T_e-w}^{R_{ref}} dq_h = \rho_m \int_{R-T_e-w}^{R_{ref}} dU, \qquad (28)$$

and if the reference surface is chosen as having a constant pressure and potential at the origin, then this can be expressed as

$$q_h(R - T_e - w) = \rho_m U(R - T_e - w) - \rho_m U(0) + q_h(0). \quad (29)$$

Since $q_h(0)$ and $U(0)$ are constants, they do not give rise to lateral variations in lithospheric deflection when the load is decomposed in the spectral domain. When the effective elastic thickness is smaller than the crustal thickness T_c, the hydrostatic pressure produced by the fluid mantle is here presumed to act directly on the base of the crust. In this case, the pressure is given by the expression

$$q_h(R - T_c - w) = \rho_m U(R - T_c - w) + \text{constant}. \qquad (30)$$

The total load p acting on the lithosphere can finally be expressed as

$$
\begin{aligned}
p = &-\frac{1}{R^2}\sum_{j=1}^{N_L}\rho(r_j)r_j^2\left[U(r_{j+1}) - U(r_j)\right] \\
&-\begin{cases} \rho_m U(R - T_e - w) + \text{constant} & \text{if } T_e > T_c \\ \rho_m U(R - T_c - w) + \text{constant} & \text{if } T_e \le T_c. \end{cases}
\end{aligned}
\qquad (31)
$$

Here, $j = 1$ refers to the base of the lithosphere, and $\rho(r_j)$, r_j, $U(r_j)$ and $U(r_{j+1})$ depend implicitly upon θ and ϕ.

2.2.3. Determination of the Lithospheric Deflection

[44] Following *Turcotte et al.* [1981], we define the parameters

$$\tau = \frac{ET_e}{R^2}, \qquad (32)$$

and

$$\sigma = \frac{D}{R^4} = \frac{\tau}{12(1 - \nu^2)}\left(\frac{T_e}{R}\right)^2. \qquad (33)$$

Along with the relationship $\nabla^2 Y_\ell^m = -\ell(\ell + 1) Y_\ell^m$, equation (22) can be expressed in the spectral domain as

$$
\begin{aligned}
\sigma\left[\ell^3(\ell+1)^3 - 4\ell^2(\ell+1)^2\right] &+ \tau[\ell(\ell+1) - 2]w_{\ell m} \\
&= [\ell(\ell+1) - (1 - \nu)]p_{\ell m},
\end{aligned}
\qquad (34)
$$

where $p_{\ell m}$ and $w_{\ell m}$ are the spherical harmonics coefficients of p and w. Since p explicitly depends upon w, we solve equations (31) and (34) in an iterative manner. First, we assume that the deflection w is zero, and then calculate the load using equation (31) and the corresponding deflection using equation (34). Next, using this approximation of the deflection, we improve our estimates of the load and deflection using equations (31) and (34). We continue iterating until the deflection converges to a stable value.

2.2.4. Treatment of the Degree 1 and 2 Topography

[45] Special care must be taken with the degree 1 and 2 terms of the topography, as these may have a different origin than our presumed loading model. The degree-1 topography is here assumed to be isostatically supported, and thus the corresponding degree-1 Moho relief was chosen such that the degree-1 gravity field is zero, as is required to be in center of mass coordinates. In contrast, *McGovern et al.* [2002] treated this term as a load, and thus the higher topography of the southern highlands was assumed to have a density equal to that of the load.

[46] The J_2 term of the gravity and topography contains a large component directly related to the hydrostatic flattening of the planet. When computing our flexure models, only 5% of the topographic J_2 term was assumed to be due to the load [e.g., *Zuber and Smith*, 1997] and after the deflections were determined, the remaining 95% of the relief was added to all density interfaces. We note that the difference in removing 90%, 95%, or 99% of this term has little influence on the results presented below.

2.3. Modeling of the Subsurface Load

[47] We parameterize the subsurface load to be proportional to the surface load by a factor f and consider two probable cases that are determined by its sign: either the load is a positive density anomaly in the crust (such as a magmatic intrusion) or a density deficit in the mantle (such as a plume or depleted mantle composition). By definition, the two loads are in phase, and the ratio f is defined by

$$f = \frac{\Delta\rho M}{\rho_l h_l}, \qquad (35)$$

where M and $\Delta\rho$ are the thickness and density anomaly of the subsurface load, and $h_l = h - w$ and ρ_l are the thickness and density of the surface load (see the schematic representation in Figure 1). If $f < 0$, a positive density perturbation is located exclusively in the crust with a thickness $M = T_c$. In contrast, if $f > 0$, then a negative density perturbation is located in the mantle. For this latter case, the value of the subsurface load thickness was set to a single value, $M = 250$ km, as exploring all possible values of M would be too time consuming from a computational point of view. This value approximately corresponds to the expected depth of melting within a plume beneath the Tharsis province [e.g., *Kiefer*, 2003]. Furthermore, a subsurface load located at depths any greater than this would likely be nearly compensated [e.g., *Zhong*, 2002].

2.4. Admittance Localization

[48] Localized admittance and correlation spectra were calculated by windowing the gravity signal and surface topography with the band-limited localization windows of
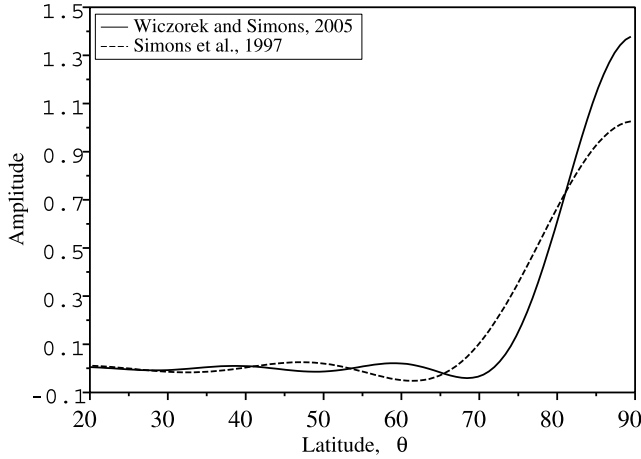
Figure 2. Spatial representation of the band-limited localization window of *Wieczorek and Simons* [2005] (solid line) and the spectrally truncated spherical cap window of *Simons et al.* [1997] (dashed line) for an angular radius of $\theta_0 = 15°$. For the first, $L_{win} = 16$, and the concentration factor is 98.8%. The second corresponds to $L_{win} = 15$ and possesses a concentration factor of 90.1%.

Wieczorek and Simons [2005]. For a given region of interest, here represented as a spherical cap, the quality of spatial localization of these windows depends exclusively upon its spectral bandwidth, L_{win}. This value was here chosen such that ~99% of the window's power was concentrated within the region of interest. Figure 2 displays the shape of this window and compares it to the equivalent spectrally truncated spherical cap window of *Simons et al.* [1997] that was subsequently used by *McGovern et al.* [2002]; *Lawrence and Phillips* [2003]; *Smrekar et al.* [2003] and *Hoogenboom et al.* [2004]. The windows represented here both correspond to a spatial diameter of $\theta_0 = 15°$ and the spatial concentration of these are 98.8% for the window of *Wieczorek and Simons* [2005] and 90.1% for the window used in *McGovern et al.* [2002].

[49] Localized spectral and cross-spectral estimates of $r(\theta, \phi)$ and $g(\theta, \phi)$ are obtained by multiplying these by the localizing window $h_w(\theta, \phi)$ in the space domain, and then expanding the resultant fields in spherical harmonics. If Ψ and Γ are the localized fields of $r(\theta, \phi)$ and $g(\theta, \phi)$ in the space domain, respectively,

$$\Psi(\theta, \phi) = r(\theta, \phi) \, h_w(\theta, \phi), \qquad (36)$$

$$\Gamma(\theta, \phi) = g(\theta, \phi) \, h_w(\theta, \phi), \qquad (37)$$

then the localized cross-spectral power $S_{\Psi\Gamma}$ is

$$S_{\Psi\Gamma}(\ell) = \sum_{m=-\ell}^{\ell} \Psi_{\ell m}\Gamma_{\ell m}, \qquad (38)$$

where $\Psi_{\ell m}$ and $\Gamma_{\ell m}$ are the spherical harmonics coefficients of Ψ and Γ, respectively. The admittance, the correlation,

and the variance of the admittance are respectively defined by:

$$Z_\ell = \frac{S_{\Psi\Gamma}(\ell)}{S_{\Psi\Psi}(\ell)}, \qquad (39)$$

$$\gamma_\ell = \frac{S_{\Psi\Gamma}(\ell)}{\sqrt{S_{\Psi\Psi}(\ell)S_{\Gamma\Gamma}(\ell)}}, \qquad (40)$$

$$\sigma_Z^2(\ell) = \frac{S_{\Gamma\Gamma}(\ell)}{S_{\Psi\Psi}(\ell)}\left(\frac{1-\gamma_\ell^2}{2\ell}\right). \qquad (41)$$

The expression for the uncertainty of the admittance implicitly assumes that $\Gamma_{\ell m} = Z_\ell \Psi_{\ell m}$ and that a correlation less than 1 is a result of noise. The correlation function varies between 1 and −1 for correlated and anti-correlated data, respectively. We note that some authors prefer to calculate the coherence function, which is generally defined as the square of our correlation function.

[50] As each windowed admittance at degree ℓ is influenced by all degrees in the range $|\ell - L_{win}| \le \ell \le \ell + L_{win}$ [*Simons et al.*, 1997; *Wieczorek and Simons*, 2005], we have considered a restricted range of wavelengths in our misfit calculations. Firstly, since the degree-2 term is mainly associated with the rotational flattening of the planet, and the first 6 degrees are largely a result of the Tharsis rise which may possess an elastic thickness that is different than the superposed volcanoes [e.g., *Zuber and Smith*, 1997; *Phillips et al.*, 2001; *Wieczorek and Zuber*, 2004], we only considered the degrees $\ell > L_{win} + 6$. Secondly, as the gravity model is only reliable to about degree 65, only the degrees $\ell \le 65 - L_{win}$ were employed.

[51] The choice of the window diameter is a rather subjective choice, and window sizes were chosen here to minimize the contribution from the Utopia mascon to the Elysium rise, the Tharsis contribution to Olympus Mons and Alba Patera, and to isolate the individual Tharsis Montes. For relatively isolated features, such as Olympus Mons, Alba Patera and the Elysium rise, we chose a window possessing an angular radius of 15°, corresponding to a bandwidth of $L_{win} = 16$. For the Tharsis Montes, which are very close to each other, we chose a value of 10° corresponding to $L_{win} = 25$. Figure 3 shows the locations of the volcanoes investigated here, as well as the size of the employed localization windows.

[52] We note that our loading model, for which the load and deflection are in phase, requires a correlation close to unity (the correlation is always greater than 0.99 for our forward models).This condition is satisfied for all volcanoes with the exception of Alba Patera at large ℓ, and to a lesser extent for Elysium where the observed correlation is only 0.95 for $\ell > 30$. For Alba Patera we have only considered degrees up to $\ell = 35$ in our misfit calculations, whereas for Elysium, we have used the entire range. Examples of observed admittance and correlation spectra are displayed in Figure 4.

[53] As described below, we calculated the reduced χ^2 and marginal probability distributions associated with the observed and theoretical admittance spectra in order to
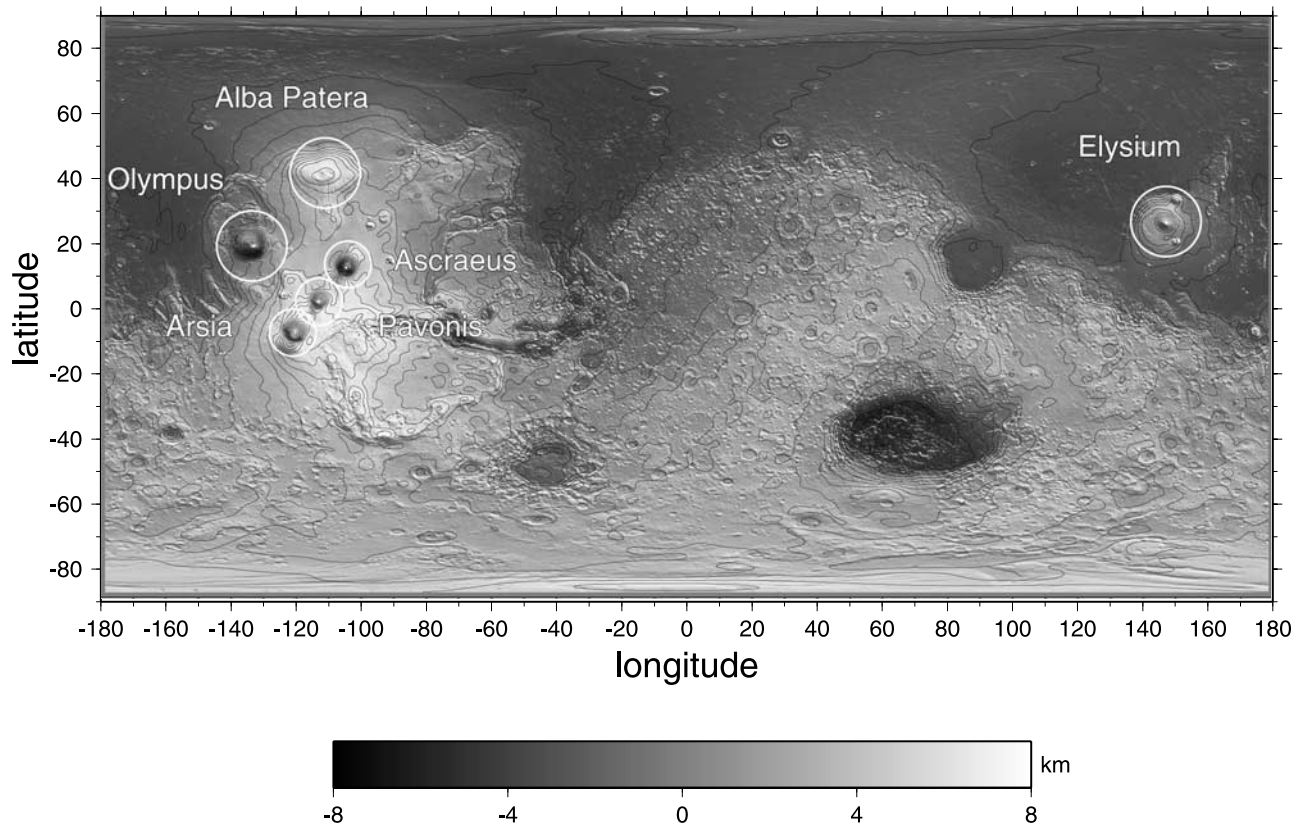
Figure 3. Position and size of the localization windows used in this study superimposed on a global topographic map on Mars.

quantify the acceptable range of parameters. Table 2 summarizes all the parameter values used in this study. The assumed mantle density is 3500 kg m^{-3}, which is consistent with the geochemical models of *Sohl and Spohn* [1997] and *Bertka and Fei* [1998]. Finally, we note that even though the free-air admittance is generally a negative quantity given our sign convention for the gravity field, for clarity, we plot the absolute value of this function.

3. Results

3.1. Comparison With Other Methods

[54] The main difference between our method and that of previous studies lies in how we calculate the load acting on the lithosphere. Previous studies have used a variety of simplifying assumptions in order to calculate this, and we show in Appendix D how the load expressions of *Turcotte et al.* [1981], *Banerdt* [1986] and *McGovern et al.* [2002] are related to our equation (31). For comparison, Figure 5 displays the predicted gravity signal of Elysium Mons using our technique as well as those of *Turcotte et al.* [1981], *Banerdt* [1986] and *McGovern et al.* [2002]. We note that the equations of Appendix D are used only to compute the load and corresponding deflections, and once the deflection is computed, the same method for calculating the gravity anomaly is used. In contrast, the studies of *Turcotte et al.* [1981] and *Banerdt* [1986] used a first order mass sheet approximation when calculating the geoid and gravity signals.

[55] The errors associated with the different approximations used in previous methods for calculating the load

magnitude depend upon the values of T_e, ρ_c and ρ_l. Figure 5 first shows that the methods of *Turcotte et al.* [1981], *Banerdt* [1986] and *McGovern et al.* [2002] give approximately the same result when the load and crustal density are the same, and that the differences among these are greatest when the elastic thickness is small, or when the density is high. Secondly, we note that the load equations used in these previous studies are not explicitly valid when the load density differs from that of the crust (see Appendix D). In order to take this case into account, *McGovern et al.* [2002] simply replaced the term ρ_c by ρ_l in equation (D6) when computing the lithospheric load and the associated deflection. This approach, however, neglects the density contrast between the load and the crust, and uses an incorrect density contrast between the crust and the mantle. We use this approach to compute the magnitude of the load and deflection when $\rho_l \neq \rho_c$ for the previous methodologies, noting that *Turcotte et al.* [1981] and *Banerdt* [1986] never explicitly considered this case. If one models the difference between the load and crustal density as was done in *McGovern et al.* [2002], then it is seen that the predicted gravity signal can differ significantly from our method. When $T_e = 10$ km, $\rho_c = 2900$ kg m^{-3} and $\rho_l = 3200$ kg m^{-3} the difference is approximately 30%.

3.2. Surface Loading Results

[56] In order to reduce the amount of computation time and to more fully explore the model parameter space, we first consider the case where only surface loads are present (the addition of subsurface loads will be considered in section 3.3). Theoretical gravity fields were calculated as
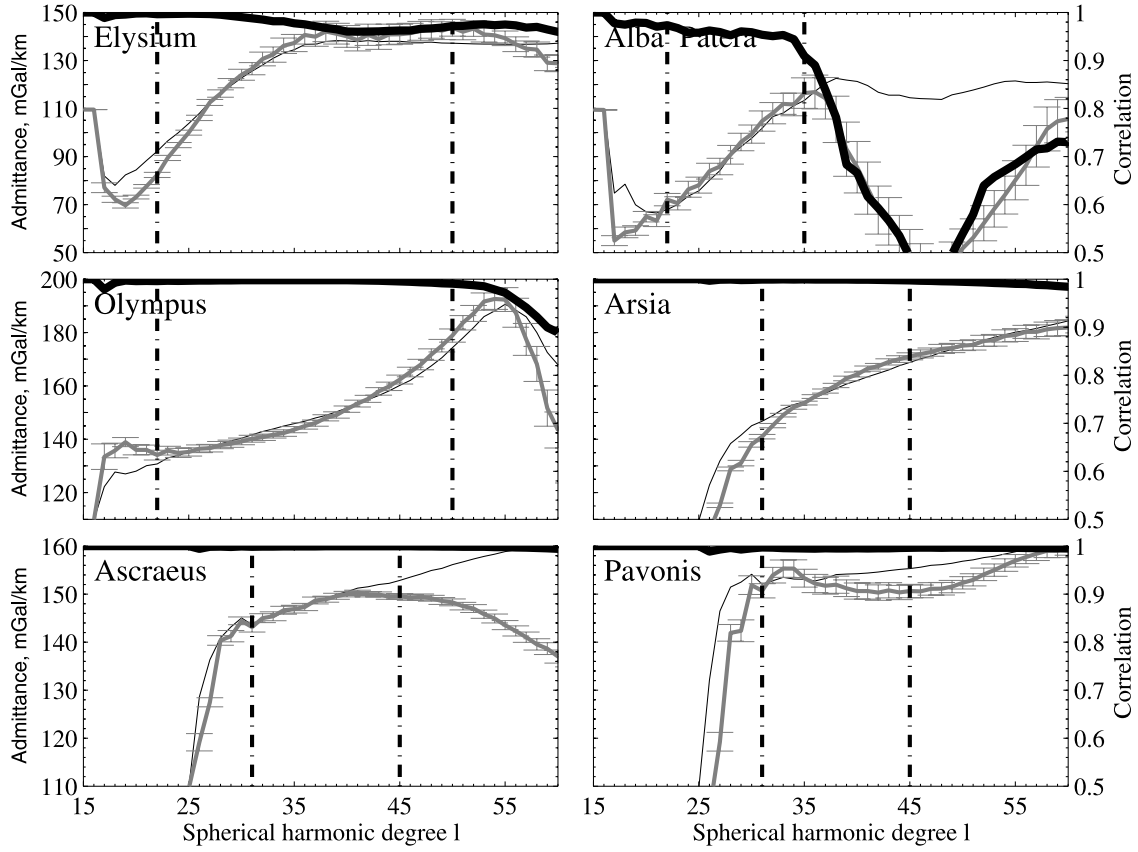
Figure 4. Left axis: gravity/topography localized admittance as a function of spherical harmonic degree ℓ for Elysium, Olympus Mons, and Alba Patera (L_{win} = 16, θ = 15°) and for the Tharsis Montes (Pavonis, Ascraeus, and Arsia; L_{win} = 25, θ = 10°). The gray curve corresponds to the observed admittance with associated uncertainties, the light black curve corresponds to the best fit model for f = 0, and the vertical dashed lines correspond to the interval used in the misfit calculation. Right axis (heavy black line): Spectral correlation γ.

a function of crustal density ρ_c, crustal thickness T_c, load density ρ_l, and elastic thickness T_e. In contrast to previous studies that have only investigated the misfit between the observed and modeled admittance by varying two parameters while keeping the others fixed, we have exhaustively explored this four-dimensional parameter space using the range or parameter values listed in Table 2 (for this case, f was set to zero). The topographic model used in this study is Mars2000.shape [*Smith et al.*, 2001], and the employed gravity model is jgm85h02 [*Lemoine et al.*, 2001]. Though the coefficients of the gravity field are given up to degree 85, we only interpret these fields up to degree 60 as their correlation dramatically decreases after this value. We then calculated the localized admittance and correlation spectra for the major Martian volcanoes: Olympus Mons, Alba Patera, the three Tharsis Montes (Arsia, Pavonis and Ascraeus) and the Elysium rise. As an example, Figure 4 shows the observed admittance and correlation spectra, as well as the best fit admittance spectrum that we have obtained for each volcano. In general, our best fit models match the observed admittances well, validating the assumption of a simple surface loading model. The major exceptions are Arsia and Elysium, where the low angular degrees are not well modeled. We will show in section 3.3 that the misfit for these low degrees decreases with the inclusion of subsurface loads.

[57] We quantify the permissibility of our models in two ways. First, in order to quantify the quality of fit between the observed and theoretical admittances, we calculated for each model the chi-squared function [e.g., *Press et al.*, 1992, chap. 15]

$$\chi^2(\rho_c, \rho_l, T_e, T_c) = \sum_{\ell=L_{win}+7}^{L_{obs}-L_{win}} \left(\frac{Z_\ell^{obs} - Z_\ell^{calc}(\rho_c, \rho_l, T_e, T_c)}{\sigma_\ell} \right)^2, \quad (42)$$

where Z_ℓ^{obs} and Z_ℓ^{calc} are the observed and modeled admittances for a given degree ℓ, σ_ℓ is the uncertainty associated with each observed admittance (see equation (41)), and $\nu = L - p$ is the number of degrees of freedom, where L is the number of degrees considered ($L_{obs} - 2L_{win} - 6$) and p is the number of model parameters, which in our case is four. If the model is an accurate representation of the underlying physical process and if the measurement errors are Gaussian, then the expectation of the reduced chi-squared function, χ^2/ν, is unity with a standard deviation of

$$\sigma_{\chi^2/\nu} = \sqrt{2/\nu}. \quad (43)$$

In the following figures, we have plotted the minimum value of $\chi^2(\rho_c, \rho_l, T_e, T_c)/\nu$ as a function of a single parameter. Second, we plot the marginal probability for a given
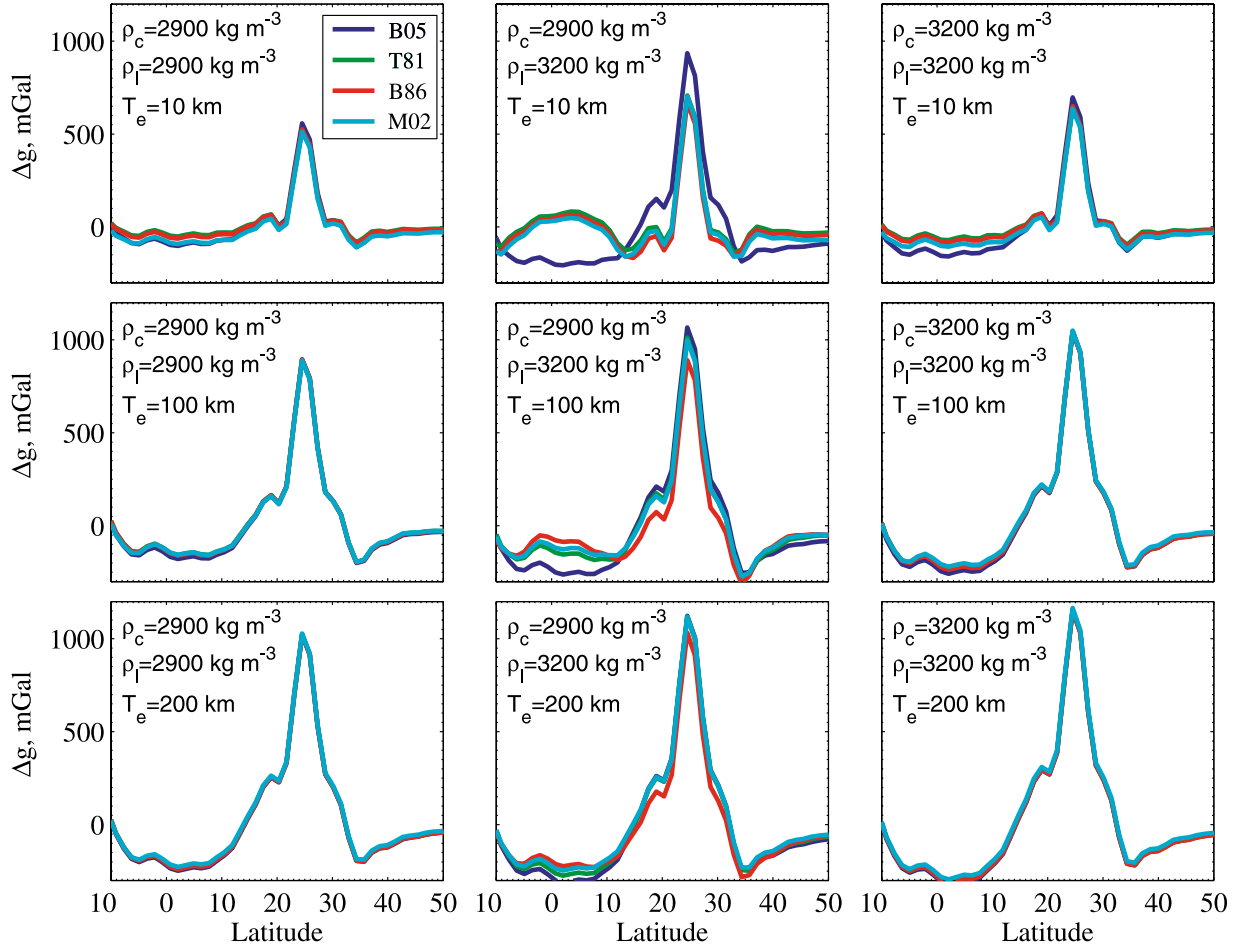
Figure 5. North-south profiles of the modeled gravity signal in the region of Elysium ($\phi = 147°$) obtained using the expressions for the surface load p described in this study (B05), *Turcotte et al.* [1981] (T81), *Banerdt* [1986] (B86), and *McGovern et al.* [2002] (M02). The results for three values of T_e (10, 100, and 200 km) are shown, as well as three sets of load and crustal densities ($\rho_c = \rho_l = 2900$ kg m^{-3}; $\rho_c = 2900$ kg m^{-3} and $\rho_l = 3200$ kg m^{-3}; $\rho_c = \rho_l = 3200$ kg m^{-3}).

parameter (the probability that a parameter X_i possesses a value x regardless of the value of the other parameters). This is given by [e.g., *Tarantola*, 1987]

$$P(X_i = x) = C \sum_{j,k,t} \exp\left[-\frac{1}{2} m(X_i, X_j, X_k, X_t)\right], \quad (44)$$

where $m(X_i, X_j, X_k, X_t)$ is the average misfit between the observed and theoretical admittance spectra

$$m(X_i, X_j, X_k, X_t) = \frac{1}{L} \sum_{\ell=L_{win}+7}^{L_{obs}-L_{win}} \left(\frac{Z_\ell^{obs} - Z_\ell^{calc}\left(\rho_{l_i}, \rho_{c_j}, T_{E_k}, T_{C_t}\right)}{\sigma_\ell}\right)^2, \quad (45)$$

and C is a constant obtained by normalizing the sum of the probabilities to 1. We use a single average misfit in equation (45), as opposed to adding each misfit in quadrature, because the Z_ℓs are not linearly independent as result of the windowing procedure. The minimum values of χ^2/ν are mainly used to quantify the

appropriateness of the model assumptions, as an acceptable model is required to have $\chi^2/\nu \sim 1$. In contrast, marginal probabilities will be used to estimate most probable parameter values and their associated uncertainties. When the width of the distribution cannot be accurately estimated because it is smaller than the sampling interval of the parameter, we conservatively quote the uncertainty as the sampling interval.

[58] Figures 6 to 9 display the minimum χ^2/ν and the marginal probability distribution as a function of a single parameter. For all volcanoes, except Elysium and Arsia, the value of the minimum χ^2/ν is close to 1, implying that a simple elastic support model of a surface load is consistent with the data. In the case of Elysium and Arsia, the minimum χ^2/ν is considerably higher ($\sim$3 for Elysium and $\sim$9 for Arsia). Figure 4 shows that the admittance function is a poor fit to the data at the lowest angular degrees for these two volcanoes, suggesting the need of incorporating subsurface loads in the admittance model.

3.2.1. Constraints on the Load Density

[59] Figure 6 shows the minimum reduced χ^2 and the marginal probability distribution as a function of the load density. With the exception of Alba Patera, ρ_l appears to be well constrained with a value of $\rho_l = 3200 \pm 100$ kg m^{-3}.
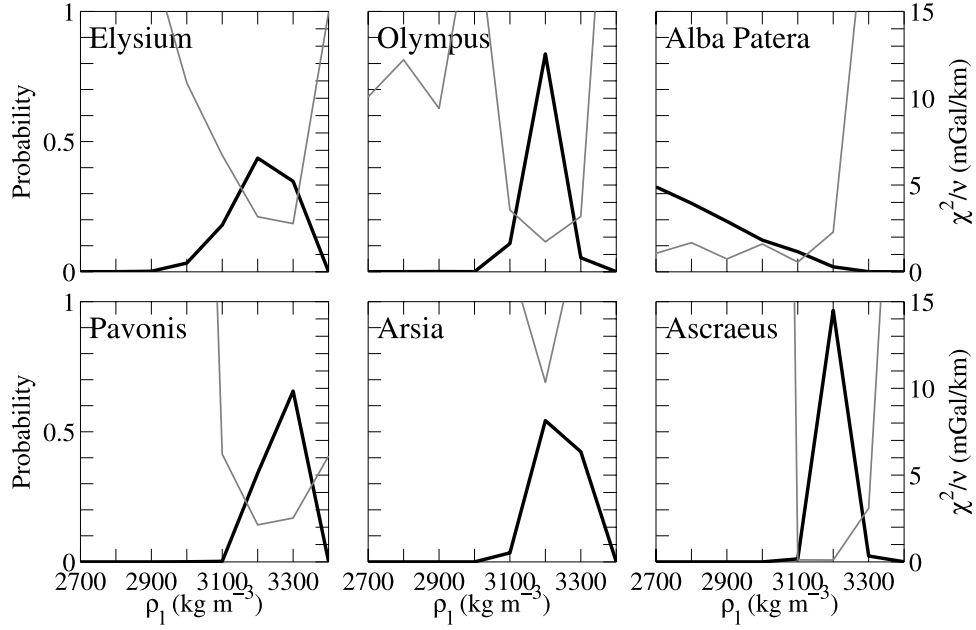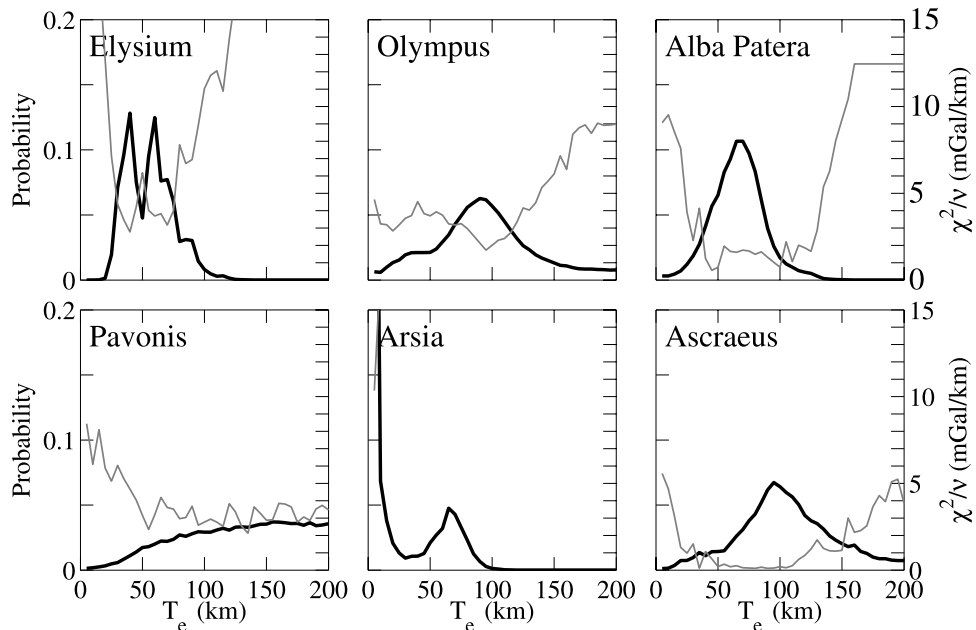
Figure 6. Left axis: Marginal probability (black bold curve) as a function of ρ_l. Right axis: Minimum χ^2/ν (gray light curve) as a function of ρ_l.

While the marginal probability distribution is not peaked for Alba Patera, lower densities are implied, and there is a 98% probability that the density is less than 3100 kg m^{-3}. Nevertheless, we note that there are models that can fit the data to within 1-σ for any value of ρ_l less than 3100 kg m^{-3}.

### 3.2.2. Constraints on the Elastic Thickness

[60] Figure 7 shows our results for the elastic thickness. The marginal probability distributions are somewhat peaked for most of the volcanoes, implying an elastic thickness of 56 ± 20 km for the Elysium rise, 93 ± 40 km for Olympus

Mons, 66 ± 20 km for Alba Patera, and 105 ± 40 km for Ascraeus Mons. For Pavonis Mons, the elastic thickness is not constrained and the marginal probability and minimum χ^2/ν are nearly flat for $T_e > 50$ km. For Arsia Mons, the probability distribution is somewhat bi-modal, with the largest mode being for near-zero elastic thicknesses. We do not have much confidence in this latter result as our best fitting model does not reproduce well the observed admittances for the lowest degrees and χ^2/ν is here much greater than 1. As will be shown in the next section, subsurface

Figure 7. Left axis: Marginal probability (black bold curve) as a function of T_e. Right axis: Minimum χ^2/ν (gray light curve) as a function of T_e.
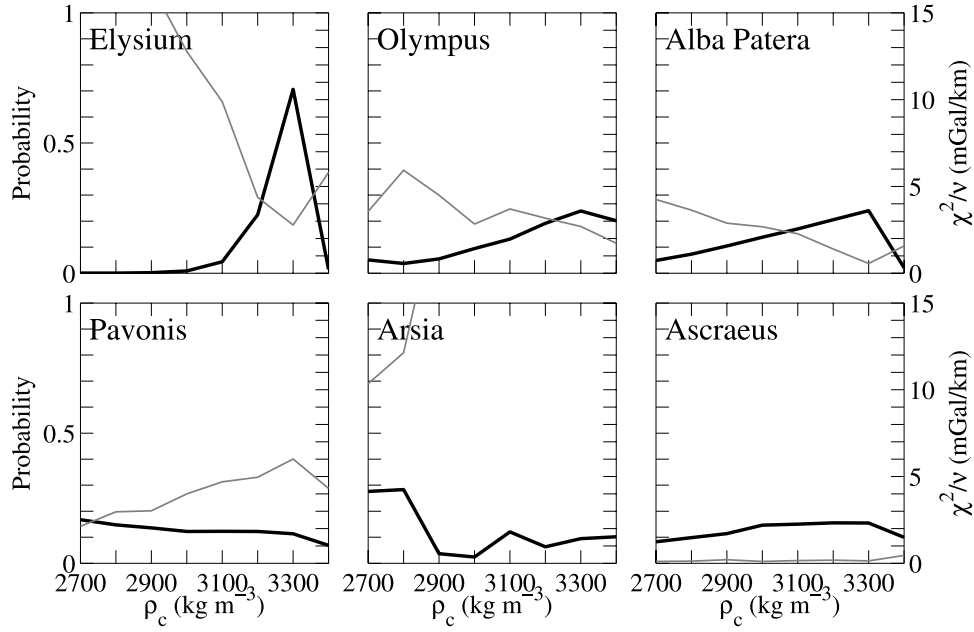
Figure 8. Left axis: Marginal probability (black bold curve) as a function of ρ_c. Right axis: Minimum χ^2/ν (gray light curve) as a function of ρ_c.

loads (such as a mantle plume) are required in order to model the low-degree portion of the admittance spectrum for this volcano.

3.2.3. Constraints on the Crustal Density and Crustal Thickness

[61] Figure 8 shows that the crustal density is only constrained for the Elysium rise with a value of $\rho_c = 3270 \pm 150$ kg m^{-3}. However, even if less constrained, similar high values of crustal density for Olympus Mons and Alba Patera seem to be implied. There is a 98% probability that $\rho_c > 3000$ kg m^{-3} for Olympus Mons, whereas for Alba Patera

the minimum χ^2/ν corresponds to $\rho_c = 3300$ kg m^{-3}. Figure 9 shows that the crustal thickness is not constrained for any of the volcanoes. These results are summarized and compared with those of *McGovern et al.* [2004] in Table 3.

3.3. Top and Bottom Load Results

[62] In this section, we explore the consequences of subsurface density anomalies within either the crust or mantle on the modeled admittance spectrum (confer with Figure 1). As the results above demonstrate that the crustal thickness is not constrained, and since a full exploration of
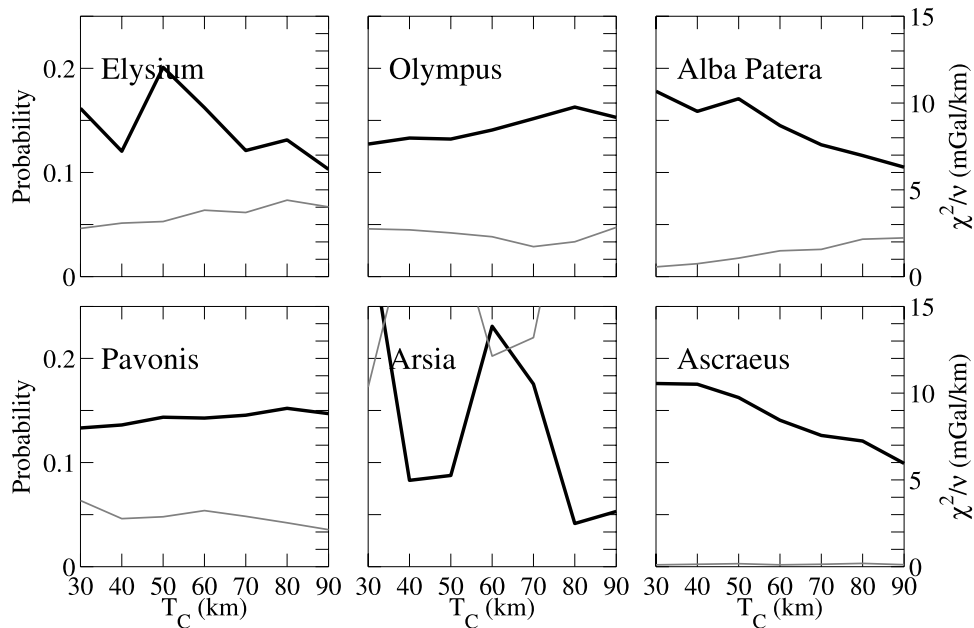
Figure 9. Left axis: Marginal probability (black bold curve) as a function of T_c. Right axis: Minimum χ^2/ν (gray light curve) as a function of T_c.

Table 3. Summary of Results and Comparison With *McGovern et al.*, [2004]

| | | This Study | | | | McGovern et al. [2004] | | |
| | | ρ_l, kg m^{-3} | | T_e, km | | | | |
Volcano	θ_0	f = 0	f ≠ 0	f = 0	f ≠ 0	θ_0	ρ_l, kg m^{-3}	T_e, km
Elysium	15°	3210 ± 180	>2900	56 ± 20	<175	17°	3250	15−45
Olympus	15°	3194 ± 110	3252 ± 150	93 ± 40	>70	17°	3150	>70
Alba Patera	15°	<3100	<3300	66 ± 20	73 ± 30	17°	2950	38−65
Pavonis	10°	3266 ± 120	–	>50	>50	11.5°	3250	<100
Arsia	10°	3240 ± 130	3300 ± 100	<30	<35	11.5°	3250	2−80
Ascraeus	10°	3200 ± 100	>2900	105 ± 40	>50	11.5°	3300	>20

the five dimensional model space is computationally infeasible, we chose here to keep this parameter fixed with a value of T_c = 50 km [e.g., *Wieczorek and Zuber*, 2004]. All other parameters were varied according to the values listed in Table 2. Figure 10 displays the minimum χ^2/ν and marginal probability as a function of f. In general, the inclusion of subsurface loads tends to decrease the value of the minimum χ^2/ν as a result of a better fit to the lowest angular degrees of the admittance function. For Elysium and Arsia, which were poorly modeled in the case of surface-only loads, the addition of subsurface loads in the mantle considerably improves the agreement between model and observation, with values of the minimum χ^2/ν now being close to unity. Figure 11 shows the improvement of the best fit modeled admittance when subsurface loads are considered. The most probable value of f for Elysium is $f = 0.1 \pm 0.06$ and for Arsia, $f = 0.25 \pm 0.1$. By definition, a positive value of f corresponds to the presence of less dense material in the mantle, which could be due to a higher temperature and/or depleted mantle composition.

[63] For the other volcanoes, Figure 10 shows that the value of f is less well constrained. Nevertheless, some trends exist and better results are generally obtained for $f > 0$. For Olympus Mons and Alba Patera, the marginal probability gives $f = 0.22 \pm 0.16$ and 0.2 ± 0.16, respectively. For Pavonis, the marginal probability increases for $f < 0$,

suggesting the presence of more dense material located in the crust. For Ascraeus, the distribution is irregular, but shows preferred values near $f = 0$.

[64] The inclusion of subsurface loads tends, in general, to enlarge the uncertainties on the other parameters. With the exception of Alba Patera, the load densities are still constrained to be about 3200 kg m^{-3}, although the uncertainty is now somewhat larger (~200 kg m^{-3} compared to ~100 kg m^{-3} found in the previous section, see Table 3). The most important change is for the elastic thickness, where only an upper or lower bound is obtained. The sole exception is Alba Patera where T_e is found to be 73 ± 30 km (both the mean value and error are slightly larger than the values obtained assuming $f = 0$). For Elysium and Arsia Montes, our results give only an upper limit, with $T_e < 150$ and $T_e < 50$ km, respectively. For Olympus Mons, Pavonis and Ascraeus Montes, only values lower than 50 km are excluded. For the crustal density, results are similar to those obtained with only surface loads, with only the density for Elysium Mons being clearly constrained with a value of ~3300 kg m^{-3}.

4. Discussion

[65] For all volcanoes investigated here, with the exception of Alba Patera, we find that the best constrained
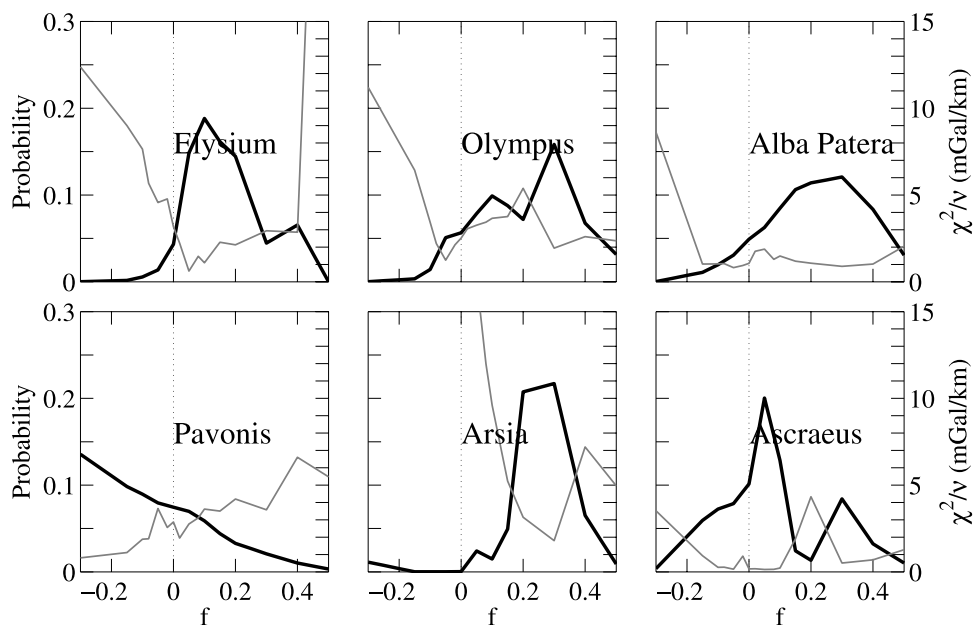
Figure 10. Left axis: Marginal probability (black bold curve) as a function of f. Right axis: Minimum χ^2/ν (gray light curve) as a function of f. The vertical dotted line emphasizes the case $f = 0$.
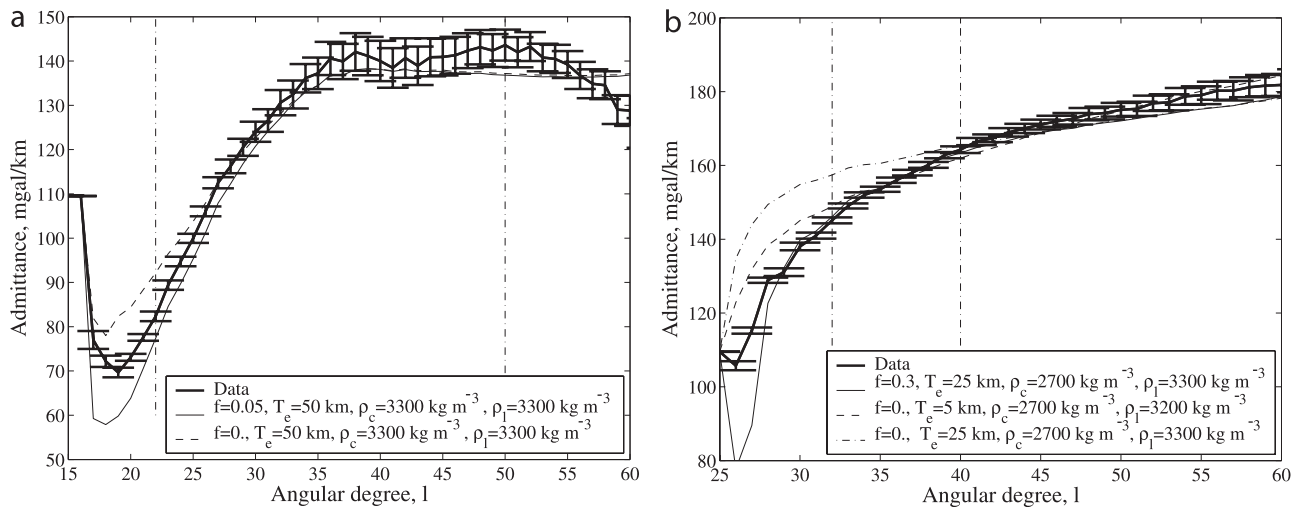
Figure 11. (a) Observed and best fit modeled admittance spectra for Elysium when $f = 0$ and $f = 0.05$. (b) The same for Arsia with $f = 0$ and $f = 0.3$.

parameter is the load density, which possesses a value of 3200 ± 100 kg m^{-3} for the case of surface-only loads. This is considerably larger than previously published values of about 2900 kg m^{-3} [*McGovern et al.*, 2002; *McKenzie et al.*, 2002], but is consistent with the corrected values of *McGovern et al.* [2004] (see Table 3 for a comparison). These high densities are in agreement with those of the Martian basaltic meteorites, which are believed to come either from the Tharsis or Elysium regions [e.g., *McSween*, 1985; *Head et al.*, 2002]. As shown in *Neumann et al.* [2004], bulk pore-free densities of these meteorites, which were calculated from estimated modal mineral abundances that are stable at the surface, lie between 3220 and 3390 kg m^{-3}. While few in situ density measurements of the Martian meteorites are available [*Britt and Consolmagno*, 2003], they are consistent with the values of *Neumann et al.* [2004]. A typical value for the porosity of the Martian meteorites is $\sim$5% [*Britt and Consolmagno*, 2003], and this would lead to a reduction of Neumann et al.'s calculated densities by $\sim$150 kg m^{-3} if the pore space was filled with air. If instead the pore space was filled with liquid water or ice, then the bulk density would only be reduced by $\sim$100 kg m^{-3}. For comparison, we note that the porosity of Hawaiian lavas is typically less than 5% at depths greater than 1 km [*Moore*, 2001]. After accounting for a reasonable density reduction due to porosity of 100 kg m^{-3}, the range of densities of the Martian meteorites (3120–3290 kg m^{-3}) is found to be nearly identical to the values obtained from this geophysical study (3200 ± 100 kg m^{-3}). As the load density is relatively constant for the volcanoes studied here, this suggests that similar magmatic process have operated at each of these regions. The lower most probable densities obtained for Alba Patera (less than 3100 kg m^{-3}) might imply that its composition is less iron-rich than the known Martian meteorites. Alternatively, given the low values of the correlation function for this volcano at high degrees, it is possible that uncorrelated subsurface loads might be important for this volcano, and that neglecting such a process could have biased our results there [e.g., *Forsyth*, 1985].

[66] Our elastic thickness estimates are found to be consistent with the revised values of *McGovern et al.*

[2004] within their respective uncertainties (see Table 3). Nevertheless, we note that our best fit values are generally larger than those of *McGovern et al.* [2004] and our uncertainties are considerably different. For instance, only a lower bound on the elastic thickness for Olympus Mons was obtained in their study ($T_e > 70$ km), whereas our estimate is somewhat better constrained (93 ± 40 km). Furthermore, while they obtained only an upper bound for Pavonis Mons ($T_e < 100$ km), we find that the elastic thickness is not constrained for this volcano.

[67] Several possibilities could explain the differences between our study and that of *McGovern et al.* [2004]. First, this could be in part a result of our more accurate technique for calculating the load acting on the lithosphere. Figure 5 demonstrates that the various approximations employed in previous studies could lead to significant errors in the modeled gravity anomaly. In particular, we have shown that the largest differences occur for low values of T_e, and when ρ_l differs from ρ_c. Second, we have computed functional misfits for a four-dimensional parameter space, whereas in *McGovern et al.* [2002], misfits were calculated only as a function of two parameters while keeping the other two fixed. Many parameters in elastic thickness modeling are correlated, and by adding more degrees of freedom to the inversion it should come as no surprise that fewer parameters will be constrained and that their respective uncertainties will be larger [see also *Lawrence and Phillips*, 2003]. Third, we have used a better localization window when calculating the localized admittance and correlation functions. Our windows concentrate $\sim$99% of their energy within the region of interest in comparison to that of *Simons et al.* [1997] that is only concentrated at $\sim$90%.

[68] It should be emphasized that the large uncertainties associated with the elastic thicknesses of the Martian volcanoes will hinder any attempt to constrain how this rheologic parameter varies in both space and time, and this will likely reduce the utility of heat flow estimates which can be derived from these values [e.g., *McNutt*, 1984; *Solomon and Head*, 1990; *McGovern et al.*, 2002]. This result is considerably amplified when subsurface loads are taken into account.

[69] On the basis of the lack of circumferential grabens around Olympus Mons, *Thurber and Toksoz* [1978] have argued that little lithospheric deflection has occurred beneath this volcano, and that the regional elastic thickness must hence be greater than 150 km. In contrast, our value is somewhat smaller (93 ± 40 km), seemingly at odds with the tectonic constraints. *Comer et al.* [1985] have investigated whether viscous relaxation might modify this constraint, but concluded that an elastic support model with an elastic thickness of ~200 km was most likely. Nevertheless, as discussed by *Comer et al.* [1985], alternative mechanisms might act to reduce or obscure circumferential faulting around this volcano. For instance, a global thermal compressive state of the planet could have suppressed the formation of extensional fractures, or fault burial could have occurred given the large number of relatively young volcanic flows that have resurfaced large portions of the surrounding region. Dynamic support might also help to minimize the extensional stresses in the region. In support of this latter suggestion, we have highlighted the likely presence of less dense material in the mantle underlying Olympus Mons, possibly related to an active plume. It is also possible that a more sophisticated elastoviscoplastic model developed in spherical coordinates might yield slightly different tectonic constraints [see *Freed et al.*, 2001; *Albert et al.*, 2000].

[70] We have found that all parameters except T_c are well constrained for the Elysium rise. We note that this result might be related to the fact that this region is relatively isolated and far from the Tharsis plateau, whereas the other volcanoes are very close to each other and are difficult to isolate in the space domain. For the Elysium region of Mars, the crustal density is predicted to be similar to the load density with a value of 3270 ± 150 kg m^{-3}. Given the similarity among the crustal density, the load density, and the Martian meteorites, it is possible that the composition of the northern lowland crust is also similar to these meteorites. While no strong constraints exist regarding the average crustal composition and density of either the northern or southern hemispheres of Mars, one possible constraint comes from the composition of rocks measured in situ at the Mars Pathfinder site. This landing site is located in an outflow channel that originates within the highlands, and therefore rocks found there could have an origin from the ancient highlands of Mars. *Neumann et al.* [2004] have calculated the modal mineralogy of the Mars Pathfinder "soil free rock" [*Brückner et al.*, 2003] and have determined that its pore-free density is about 3060 kg m^{-3}. If this value is representative of the southern highlands crust, and if our results for the Elysium rise are typical of the northern hemisphere, then this implies that the composition of the northern hemisphere crust is considerably different than that of the southern highlands. In particular, the northern lowlands would be more dense by ~200 kg m^{-3}. This suggests the possibility that Pratt compensation (i.e., lateral density variations as opposed to crustal thickness variations) may be largely responsible for the 3.1-km center-of-mass/center-of-figure offset of the planet. Assuming an average crustal thickness for Mars between 38 and 62 km [*Wieczorek and Zuber*, 2004], the ~6 km difference in elevation between the northern lowlands and southern highlands would correspond to a difference in density between ~310 and

520 kg m^{-3}. Though slightly on the high side, this number is comparable with the difference in density between the Mars Pathfinder soil free rock (assumed to be representative of the southern highlands) and the crust beneath the Elysium rise.

[71] Given the early Noachian age of the Martian lowlands [*Frey et al.*, 2002], this density and compositional dichotomy between the two hemispheres must have formed during the earliest geologic evolution of the planet. One possible origin is an early episode of plate tectonics operating in the northern lowlands. In this scenario, the southern highlands of Mars could either represent an ancient primordial crust or the resulting products of subduction related volcanism. Alternatively, it is possible that this feature could be related to a fundamental asymmetry in the primary differentiation of this planet. For example, the nearside-farside dichotomy of the Moon appears to be related to the asymmetric crystallization of a near-global magma ocean [e.g., *Jolliff et al.*, 2000].

[72] Lastly, we emphasize that the inclusion of subsurface loads dramatically improves the model fits for the Elysium rise and Arsia Mons, where less dense materials in the mantle are required to explain the gravity and topography data. Whereas model results for Olympus Mons and Alba Patera are not noticeably improved by the addition of subsurface loads, a less dense mantle is nevertheless preferred to dense crustal intrusions. A less dense mantle beneath these volcanoes can be interpreted as being a result of thermal and/or compositional effects. In the latter case, the extraction of dense iron-rich basaltic magmas from the mantle would act to decrease its density [*Oxburgh and Parmentier*, 1977]. The contribution of these two effects can be parameterized by the relation

$$\Delta\rho = -\rho_m[\beta F + \alpha\Delta T], \qquad (46)$$

where $\Delta\rho$ and ΔT are, respectively, the density and the temperature anomalies within the mantle, ρ_m is the mean mantle density (see Table 2), α is the thermal expansion coefficient (here assumed to be 3×10^{-5} °C^{-1}), F is the degree of depletion, and β is a coefficient of density reduction due to the extraction of partial melts. In order to roughly quantify the expected density variation due to compositional effects, we set $\beta = 0.07$ [e.g., *Jordan*, 1979] and use the interval $0.02 \leq F \leq 0.12$ obtained by *Kiefer* [2003], yielding an expected density variation of ~5–30 kg m^{-3}. On the other hand, convection modeling of *Kiefer* [2003] suggest that the plume conduit beneath the Tharsis rise could be as much as ~400°C hotter than the ambient mantle. This temperature variation would correspond to a density reduction of ~40 kg m^{-3}. Combining these two effects, we would expect a mantle density reduction beneath the Martian volcanoes to be less than 70 kg m^{-3}.

[73] We next compare the above expected density variations with the magnitude of the subsurface load obtained from our admittance analysis. The density variations of our models are derived from equation (35) for a given value of f, the thickness of the "plume" M, and the thickness of the surface load h_l. Given computational constraints, only one value of M was used in our subsurface loading model ($M = 250$ km), and it should be clear that an increase (decrease) of this parameter would decrease (increase) the obtained

density anomaly by nearly the same factor. For the Elysium rise, $f = 0.1 \pm 0.06$, and the associated density variations are predicted to lie between 10 and 45 kg m^{-3}. This can be explained by either a thermal or compositional effect. For Arsia, $f = 0.25 \pm 0.1$, and this yields rather large density variations between 170 and 390 kg m^{-3}. Even the lowest of these values is much larger than the expected variations cited above, and this may imply higher temperatures and/or a higher degree of mantle depletion beneath this volcano. This might not be an unreasonable expectation as Arsia Mons is the most topographically prominent of the Tharsis Montes, and could be located directly above an active plume (the other Tharsis Montes would be off the plume axis in this scenario). Even if the value of f is not as well defined for the other volcanoes, positive values are preferred for Olympus Mons, and the variation in density is found to lie between 0 and 230 kg m^{-3}, consistent with thermal and/or composition effects.

[74] The negative density anomalies beneath the major volcanoes are most reasonably interpreted as being the result of a mantle plume. The results of this study thus imply that the mantle is not only dynamically active in the region of Tharsis and Olympus Mons, but also beneath the Elysium rise. A currently active plume is consistent with analyses of cratering statistics on Olympus Mons and the Elysium rise that suggest the presence of young lava flows ($\sim$10–30 Myr [*Hartmann and Neukum*, 2001]) and with the radiometric ages of the Shergottites that are between 175 and 475 Myr [*Nyquist et al.*, 2001]. We note the possibility that higher temperatures beneath the Tharsis rise might also be a consequence of the thermal insulation associated with a thicker than typical crust [*Breuer et al.*, 1993]. For Pavonis, we found that preferred models are obtained for $f < 0$. If our admittance model is correct for this volcano, then this implies the presence of dense intrusive materials in the crust, such as the differentiation products associated with a central magma chamber.

5. Conclusions

[75] We have presented an accurate method to analyze localized gravity/topography admittances of the major Martian volcanoes by assuming that surface and subsurface loads are elastically supported by the lithosphere. Our analysis represents an improvement over previous studies in several ways. First, our methodology computes the gravity anomaly, surface deflection, and load acting on the lithosphere in a self-consistent manner. Previous studies have not been able to correctly model the case where the load density differs from that of the crust. Secondly, we calculate localized admittance and correlation spectra using localizing windows that concentrate almost all of their energy ($\sim$99%) within the region of interest, whereas previous studies have employed sub-optimal windows that are only concentrated at about 90%. Finally we have systematically investigated the misfit function for a high dimensional space which includes the elastic thickness, crustal thickness, load density, crustal density, and ratio of subsurface to surface loading. The results we have obtained here, although consistent with those of *McGovern et al.* [2004], offer more precise and reliable bounds on the elastic thickness and load density.

[76] The main result we have obtained concerns the density of the volcanoes. With the exception of Alba Patera, we have obtained a value of 3200 $\pm$ 100 kg m^{-3} that is higher than what was previously published (i.e., 2900 $\pm$ 100 kg m^{-3} [*McKenzie et al.*, 2002; *McGovern et al.*, 2002]), but consistent with the corrected value of *McGovern et al.* [2004]. These high densities are in agreement with those of the Martian basaltic meteorites, which are believed to come from the Tharsis or Elysium volcanic province. When subsurface loads are neglected, the elastic thickness is found to be moderately constrained for Elysium (56 $\pm$ 20 km), Alba Patera (66 $\pm$ 20 km), Olympus Mons (93 $\pm$ 40 km) and Ascraeus (105 $\pm$ 105 km). However, when subsurface loads are taken into account, the uncertainties obtained are extremely large, with the exception of Alba Patera where we obtain $T_e = 73 \pm 30$ km. The crustal density is only constrained for the Elysium region ($\rho_c = 3270 \pm 150$ kg m^{-3}). Given the similarity among the crustal density, load density and Martian meteorites, it is possible that the crustal composition of the northern lowlands is similar to these meteorites. An estimate for the density of the southern highlands crust is lower [*Neumann et al.*, 2004], and this seems to indicate that the northern hemisphere crust is more mafic in composition than the southern highlands. Such a compositional difference suggests the possibility that Pratt compensation may be partially responsible for the 3.1 km center of mass/center of figure offset of the planet.

[77] Finally, we have shown that subsurface loads play an important role in the gravity and topography signal for the Elysium rise and Arsia Mons, and to a lesser extent Olympus Mons and Alba Patera. The less dense mantle beneath these volcanoes can reasonably be interpreted as an active plume which contains contribution from both thermal and compositional effects. Such an assessment is consistent with a possibility of a recent volcanism in this region as suggested by crater counting studies, as well as the ages of the basaltic Martian meteorites.

Appendix A: Mapped Coordinates

[78] In this appendix, we show how equations (1) and (2) can be expressed in terms of the mapped coordinates s, θ, and ϕ. First, by differentiating equation (3) we obtain

$$dr = a_1 ds + a_2 d\theta + a_3 d\phi, \tag{A1}$$

where

$$a_1 = \frac{r_{i+1}(\theta, \phi) - r_i(\theta, \phi)}{S_{i+1} - S_i}, \tag{A2}$$

$$a_2 = \left(\frac{s - S_i}{S_{i+1} - S_i}\right)\frac{\partial r_{i+1}}{\partial \theta} + \left(\frac{S_{i+1} - s}{S_{i+1} - S_i}\right)\frac{\partial r_i}{\partial \theta}, \tag{A3}$$

$$a_3 = \left(\frac{s - S_i}{S_{i+1} - S_i}\right)\frac{\partial r_{i+1}}{\partial \phi} + \left(\frac{S_{i+1} - s}{S_{i+1} - S_i}\right)\frac{\partial r_i}{\partial \phi}. \tag{A4}$$

In equations (A3) and (A4), r_i depends implicitly upon θ and ϕ. The transformation matrix between $(dr, d\theta, d\phi)$ and $(ds, d\theta, d\phi)$ can be written in matrix notation as

$$\begin{bmatrix} ds \\ d\theta \\ d\phi \end{bmatrix} = \begin{bmatrix} 1+b_1 & b_2 & b_3 \\ 0 & 1 & 0 \\ 0 & 0 & 1 \end{bmatrix} \begin{bmatrix} dr \\ d\theta \\ d\phi \end{bmatrix}, \quad (A5)$$

where

$$b_1 = \frac{1}{a_1} - 1, \quad (A6)$$

$$b_2 = -\frac{a_2}{a_1}, \quad (A7)$$

$$b_3 = -\frac{a_3}{a_1}. \quad (A8)$$

For a function $f(r, \theta, \phi)$, where r is a function of s, θ and ϕ, its partial derivatives with respect to r, θ and ϕ are given by

$$\frac{\partial f}{\partial r} = \frac{\partial f}{\partial s}\frac{\partial s}{\partial r} + \frac{\partial f}{\partial \theta}\frac{\partial \theta}{\partial r} + \frac{\partial f}{\partial \phi}\frac{\partial \phi}{\partial r}, \quad (A9)$$

$$\frac{\partial f}{\partial \theta} = \frac{\partial f}{\partial s}\frac{\partial s}{\partial \theta} + \frac{\partial f}{\partial \theta}, \quad (A10)$$

$$\frac{\partial f}{\partial \phi} = \frac{\partial f}{\partial s}\frac{\partial s}{\partial \phi} + \frac{\partial f}{\partial \phi}, \quad (A11)$$

where the angular partial derivatives of f on the left hand side are calculated at constant r, and those on the right at constant s. Using equation (A5), we then obtain

$$\frac{\partial f}{\partial r} = (1+b_1)\frac{\partial f}{\partial s}, \quad (A12)$$

$$\frac{\partial f}{\partial \theta} = b_2 \frac{\partial f}{\partial s} + \frac{\partial f}{\partial \theta}, \quad (A13)$$

$$\frac{\partial f}{\partial \phi} = b_3 \frac{\partial f}{\partial s} + \frac{\partial f}{\partial \phi}, \quad (A14)$$

where the same remarks concerning partial differentiation apply here as well. The relationship between the derivative operators in the two sets of coordinates can be shown to be

$$\begin{bmatrix} \dfrac{\partial}{\partial r} \\[2mm] \dfrac{\partial}{\partial \theta} \\[2mm] \dfrac{\partial}{\partial \phi} \end{bmatrix} = \mathbf{A} \begin{bmatrix} \dfrac{\partial}{\partial s} \\[2mm] \dfrac{\partial}{\partial \theta} \\[2mm] \dfrac{\partial}{\partial \phi} \end{bmatrix}, \quad (A15)$$

where the angular derivatives on the left and right sides are calculated at constant r and s, respectively, and the transformation matrix is

$$\mathbf{A} = \begin{bmatrix} 1+b_1 & 0 & 0 \\ b_2 & 1 & 0 \\ b_3 & 0 & 1 \end{bmatrix}. \quad (A16)$$

[79] Equation (1) can be rewritten in a matrix form as

$$\begin{bmatrix} G_r \\ G_\theta \\ G_\phi \end{bmatrix} = \begin{bmatrix} \dfrac{\partial}{\partial r} \\[2mm] \dfrac{1}{r}\dfrac{\partial}{\partial \theta} \\[2mm] \dfrac{1}{r\sin\theta}\dfrac{\partial}{\partial \phi} \end{bmatrix} U, \quad (A17)$$

which can be rewritten in the new set of coordinates (s, θ, ϕ) using equation (A15) as

$$\begin{bmatrix} G_r \\ G_\theta \\ G_\phi \end{bmatrix} = \begin{bmatrix} 1+b_1 & 0 & 0 \\[2mm] \dfrac{b_2}{r} & \dfrac{1}{r} & 0 \\[2mm] \dfrac{b_3}{r\sin\theta} & 0 & \dfrac{1}{r\sin\theta} \end{bmatrix} \begin{bmatrix} \dfrac{\partial U}{\partial s} \\[2mm] \dfrac{\partial U}{\partial \theta} \\[2mm] \dfrac{\partial U}{\partial \phi} \end{bmatrix}. \quad (A18)$$

From this equation, the first derivative of U with respect to s and the horizontal components of the gravity field can be written as

$$\frac{\partial U}{\partial s} = \frac{r_{i+1} - r_i}{s_{i+1} - s_i} G_r, \quad (A19)$$

$$\mathbf{G}_\Sigma = \nabla_{\Sigma_s} U - \left[\frac{s - s_i}{r_{i+1} - r_i}\nabla_{\Sigma_s} r_{i+1} + \frac{s_{i+1} - s}{r_{i+1} - r_i}\nabla_{\Sigma_s} r_i \right]\frac{\partial U}{\partial s}, \quad (A20)$$

where $\mathbf{G}_\Sigma$ corresponds to the horizontal component of the field $\mathbf{G}$, and the horizontal gradient ∇_{Σ_s} is here calculated at constant s. In θ and ϕ coordinates, the horizontal gradient operator is defined as

$$\nabla_\Sigma = \mathbf{e}_\theta \frac{1}{r}\frac{\partial}{\partial \theta} + \mathbf{e}_\phi \frac{1}{r\sin\theta}\frac{\partial}{\partial \phi}. \quad (A21)$$

Equation (2) can be explicitly written as

$$-4\pi\mathcal{G}\rho = \nabla \cdot \mathbf{G}$$
$$= \frac{\partial G_r}{\partial r} + \frac{2G_r}{r} + \frac{1}{r\sin\theta}\left[\frac{\partial}{\partial \theta}(\sin\theta\, G_\theta) + \frac{\partial G_\phi}{\partial \phi}\right], \quad (A22)$$

where the angular derivatives are calculated at constant r. Using equations (A12)–(A14), this equation can be expressed in the new set of coordinates s, θ, and ϕ, where the angular derivatives are calculated at constant s, as

$$-4\pi\mathcal{G}\rho = \nabla \cdot \mathbf{G}$$
$$= \frac{\partial G_r}{\partial s} + \frac{2G_r}{r}$$
$$+ \frac{1}{r\sin\theta}\left[\frac{\partial}{\partial \theta}(\sin\theta\, G_\theta) + \frac{\partial G_\phi}{\partial \phi}\right]$$
$$+ b_1\frac{\partial G_r}{\partial s} + \frac{b_2}{r}\frac{\partial G_\theta}{\partial s} + \frac{b_3}{r\sin\theta}\frac{\partial G_\phi}{\partial s}. \quad (A23)$$

Finally, we rearrange the above equation using equations (A6)–(A8), yielding the following expression for the first

derivative of the radial component of the gravity field with respect to s:

$$\frac{\partial G_r}{\partial s} = -\left[\frac{r_{i+1}(\theta,\phi) - r_i(\theta,\phi)}{S_{i+1} - S_i}\right]\left[4\pi\mathcal{G}\rho + \frac{2G_r}{r} + \frac{1}{r}\nabla_{\Sigma_s}\cdot\mathbf{G}_\Sigma\right]$$
$$+ \left[\frac{s - S_i}{S_{i+1} - S_i}\nabla_{\Sigma_s}r_{i+1} + \frac{S_{i+1} - s}{S_{i+1} - S_i}\nabla_{\Sigma_s}r_i\right]\cdot\frac{\partial\mathbf{G}_\Sigma}{\partial s}, \quad (A24)$$

where $\mathbf{G}_\Sigma$ is the horizontal component of the gravity field, and the horizontal divergence of the vector $\mathbf{G}$, calculated at constant s, is defined as

$$\nabla_{\Sigma_s}\cdot\mathbf{G}_\Sigma = \frac{1}{\sin\theta}\left[\frac{\partial}{\partial\theta}(\sin\theta G_\theta) + \frac{\partial G_\phi}{\partial\phi}\right]. \quad (A25)$$

Appendix B: Calculation of the Potential Exterior to a Planet

[80] The technique for determining the gravity field exterior to a planet is similar to *Wieczorek and Phillips* [1998] except that we allow for lateral variations of density. We start with Newton's law of gravitation

$$U(r,\theta,\phi) = \int_{V'}\frac{\mathcal{G}\,\rho(\mathbf{r}')\,dV'}{|\mathbf{r} - \mathbf{r}'|}, \quad (B1)$$

and the identity

$$\frac{1}{|\mathbf{r} - \mathbf{r}'|} = \frac{1}{r}\sum_{\ell=0}^{\infty}\left(\frac{r'}{r}\right)^\ell\frac{1}{2\ell+1}\sum_{m=-\ell}^{\ell}Y_\ell^m(\theta,\phi)Y_\ell^{m*}(\theta',\phi'), \quad (B2)$$

which is valid for $r > r'$. Y_ℓ^m is the complex spherical harmonic function of degree ℓ and order m whose inner product is 4π:

$$\int_\Omega Y_\ell^{m*}Y_{\ell'}^{m'}d\Omega = 4\pi\,\delta_{\ell\ell'}\,\delta_{mm'}, \quad (B3)$$

where $\delta_{ii'}$ is the Kronecker delta function which is equal to 1 when $i = i'$, and zero otherwise. The superscript * denotes complex conjugation. The spherical harmonic transform and reconstruction of an arbitrary function $u(\theta, \phi)$ is given by

$$u_{\ell m} = \frac{1}{4\pi}\int_\Omega u(\theta,\phi)\,Y_\ell^{m*}(\theta,\phi)\,d\Omega, \quad (B4)$$

$$u(\theta,\phi) = \sum_{\ell=0}^{\infty}\sum_{m=-\ell}^{\ell}u_{\ell m}Y_\ell^m(\theta,\phi). \quad (B5)$$

Substituting equation (B2) into (B1), we obtain the expression

$$U(r,\theta,\phi) = \sum_{i=1}^{N}\sum_{\ell=0}^{\infty}\sum_{m=-\ell}^{\ell}\left(\frac{1}{r}\right)^{\ell+1}\frac{1}{2\ell+1}\xi_{\ell m}^i Y_\ell^m(\theta,\phi), \quad (B6)$$

where N is the number of layers used in the density model, and

$$\xi_{\ell m}^i = \int_{\Omega'}\int_{r_i(\theta,\phi)}^{r_{i+1}(\theta,\phi)}\mathcal{G}\rho(r,\theta,\phi)(r)^{\ell+2}\,dr\,Y_\ell^{m*}(\theta,\phi)\,d\Omega. \quad (B7)$$

Equation (B6) is valid only for all points exterior to the maximum elevation of the planet. It will be useful to calculate the above integral in the coordinates s, θ, and ϕ as defined by equation (3). After a change of variables, $\xi_{\ell m}^i$ can be expressed as

$$\xi_{\ell m}^i = \int_\Omega\int_{S_i}^{S_{i+1}}\mathcal{G}\rho(s,\theta,\phi)(r)^\ell|J'|s^2ds\,Y_\ell^{m*}(\theta,\phi)\,d\Omega, \quad (B8)$$

where $|J'|$ is defined as $\frac{r^2}{s^2}|J|$, and the Jacobian determinant $|J|$ is

$$|J| = \left|\frac{\partial(r,\theta,\phi)}{\partial(s,\theta,\phi)}\right| = \frac{r_{i+1}(\theta,\phi) - r_i(\theta,\phi)}{S_{i+1} - S_i}. \quad (B9)$$

The integral over s in equations (B7) and (B8) can be computed by Gauss-Legendre quadrature on a set of grid points (θ_k, ϕ_k) and then the integral over θ and ϕ can be calculated using standard spherical harmonic transformation routines [e.g., *Lognonné and Romanowicz*, 1990; *Driscoll and Healy*, 1994; *Sneeuw*, 1994]. To facilitate this latter operation, the grid coordinates (θ_k, ϕ_k) are chosen to be equally spaced in longitude and with latitude points corresponding to the Gauss-Legendre quadrature nodes.

Appendix C: Definition of Generalized Spherical Harmonics

[81] In order to use properties similar to those of the spherical harmonics when investigating vector (or tensor) fields, we introduce here the generalized spherical harmonics, as described in detail by *Phinney and Burridge* [1973]. For a vector field $\mathbf{u}(r, \theta, \phi)$ that has components u_r, u_θ and u_ϕ, it is convenient to define the new contravariant components

$$u^- = \frac{1}{\sqrt{2}}\left(u_\theta + iu_\phi\right), \quad (C1)$$

$$u^0 = u_r, \quad (C2)$$

$$u^+ = \frac{1}{\sqrt{2}}\left(-u_\theta + iu_\phi\right), \quad (C3)$$

and the new canonical basis

$$\mathbf{e}_- = \frac{1}{\sqrt{2}}\left(\mathbf{e}_\theta - i\mathbf{e}_\phi\right), \quad (C4)$$

$$\mathbf{e}_0 = \mathbf{e}_r, \quad (C5)$$

$$\mathbf{e}_+ = \frac{1}{\sqrt{2}}\left(-\mathbf{e}_\theta - i\mathbf{e}_\phi\right), \quad (C6)$$

such that

$$\mathbf{u} = \sum_{\alpha}^{-,0,+} u^{\alpha} \mathbf{e}_{\alpha}. \tag{C7}$$

The contravariant components u^{α} can then be expanded in terms of *generalized spherical harmonics* as

$$u^{\alpha}(r, \theta, \phi) = \sum_{\ell=0}^{\infty} \sum_{m=-\ell}^{\ell} u_{\ell m}^{\alpha}(r) Y_{\ell}^{\alpha m}(\theta, \phi), \tag{C8}$$

where $Y_{\ell}^{\alpha m}(\theta, \phi)$ are the generalized spherical harmonics, and $u_{\ell m}^{\alpha}$ are the generalized spherical harmonics coefficients of the contravariant components. For a scalar field, only the $\alpha = 0$ component is required. The generalized spherical harmonics are defined as

$$Y_{\ell}^{\alpha m}(\theta, \phi) = P_{\ell}^{\alpha m}(\cos \theta) e^{im\phi}, \tag{C9}$$

where $P_{\ell}^{\alpha m}$ is the generalized Legendre function. We note that when $\alpha = 0$, P_{ℓ}^{0m} is equal to the standard associated Legendre functions P_{ℓ}^{m}. Recurrence algorithms for calculating these are given by *Phinney and Burridge* [1973]. Expressions for the gradient and divergence are given in appendix C of *Phinney and Burridge* [1973], which we quote here. For a scalar field $U(r, \theta, \phi)$, the gradient operator is defined as

$$\nabla = \mathbf{e}_{-} \nabla^{-} + \mathbf{e}_{0} \nabla^{0} + \mathbf{e}_{+} \nabla^{+}. \tag{C10}$$

The contravariant components of this operator are given by

$$\nabla^{\alpha} U(r, \theta, \phi) = \sum_{\ell=0}^{\infty} \sum_{m=-\ell}^{\ell} \frac{1}{r} \Omega_{\ell} U_{\ell m}(r) Y_{\ell}^{\alpha m}(\theta, \phi), \tag{C11}$$

$$\nabla^{0} U(r, \theta, \phi) = \sum_{\ell=0}^{\infty} \sum_{m=-\ell}^{\ell} \frac{d}{dr} U_{\ell m}(r) Y_{\ell}^{0m}(\theta, \phi), \tag{C12}$$

where $\Omega_{\ell} = \sqrt{\ell(\ell+1)/2}$, and $U_{\ell m}(r)$ are the scalar spherical harmonic coefficients at radius r. The horizontal divergence of a vector field $\mathbf{G}(r, \theta, \phi)$ is

$$\nabla_{\Sigma} \cdot \mathbf{G}_{\Sigma} = (\mathbf{e}_{+} \nabla^{+} + \mathbf{e}_{-} \nabla^{-}) \cdot \mathbf{G}_{\Sigma}, \tag{C13}$$

where $\mathbf{G}_{\Sigma}$ is the horizontal component of $\mathbf{G}$, and can be calculated using its generalized spherical harmonics coefficients by

$$\nabla_{\Sigma} \cdot \mathbf{G}_{\Sigma}(r, \theta, \phi) = -\sum_{\ell=0}^{\infty} \sum_{m=-\ell}^{\ell} \frac{\Omega_{\ell}}{r} \left[G_{\ell m}^{+}(r) + G_{\ell m}^{-}(r) \right] Y_{\ell}^{0m}(\theta, \phi), \tag{C14}$$

noting that $G_{\ell m}^{+} = G_{\ell m}^{-}$ for our case where the gravity field is both real and poloidal.

Appendix D: Relationship of the Load Equation to Previous Studies

[82] The expression for the load p given by *Turcotte et al.* [1981], *Banerdt* [1986] or *McGovern et al.* [2002] can be derived from our expressions for q_a and q_h given by equations (27) and (29) after a series of approximations. First, setting $r^2 = R^2$, and assuming that no lateral variations of density are present, the expression for q_a becomes

$$q_a = -\int_{r_2}^{r_4} \frac{\partial U}{\partial r} \rho(r) dr = -\int_{U(r_2)}^{U(r_4)} \rho(r) dU$$
$$= -\sum_{j=1}^{N} \rho(r_j) \left[U(r_{j+1}) - U(r_j) \right], \tag{D1}$$

where N is the total number of layers, r_j refers to $r(s_j)$, $j = 1$ represents the base of the lithosphere, and r_j, $\rho(r_j)$, $U(r_j)$ and $U(r_{j+1})$ implicitly depend upon θ and ϕ. As defined in Table 1, $r_2 = R - T_e - w$ and $r_4 = R + h$. We note that w is here measured positive downward. The general expression of the load $p = q_a - q_h$ (when $T_e \geq T_c$) is then

$$p = -\rho_l U(R+h) + \rho_l U(R-w)$$
$$\quad - \rho_c U(R-w) + \rho_c U(R-T_c-w)$$
$$\quad - \rho_m U(R-T_c-w) + \rho_m U(R-T_e-w)$$
$$\quad - \rho_m U(R-T_e-w), \tag{D2}$$

where ρ_l, ρ_c and ρ_m denote, respectively, the load density, the crustal density and the mantle density. When the load density is equal to the crustal density, this reduces to

$$p = -\rho_c U(R+h) - (\rho_m - \rho_c) U(R-T_c-w). \tag{D3}$$

Next, expanding the above potential to first order about R and $R - T_c$ yields

$$p = -\rho_c \left(U_0 + h \frac{dU}{dr} \right) - (\rho_m - \rho_c) \left(U_c - w \frac{dU}{dr} \right), \tag{D4}$$

where U_0 and U_c are the gravitational potentials at the surface and base of the crust, respectively. Using $dU/dr = -g_0$, where g_0 is the gravitational acceleration at the surface (here assumed to be constant within the lithosphere), the potential at the surface and crust-mantle interface is equal to $U_0 = h_g g_0$ and $U_c = h_{g_c} g_0$, where h_g and h_{g_c} are the heights of a constant potential at the surface and base of the crust respectively. The load p can then be written as

$$p = g_0 \left[\rho_c (h - h_g) - \Delta\rho (h_{g_c} + w) \right], \tag{D5}$$

where $\Delta\rho = \rho_m - \rho_c$. This equation is equivalent to that given by *Banerdt* [1986], noting that he defines w as being positive upward. If h_{g_c} is assumed to be 0, expression (D5) becomes the relation used by *McGovern et al.* [2002]:

$$p = g_0 \left[\rho_c (h - h_g) - \Delta\rho w \right]. \tag{D6}$$

If the approximation $h_{g_c} = h_g$ is used, then the relation of *Turcotte et al.* [1981] is obtained:

$$p = g_0 \left[\rho_c h - (\rho_m - \rho_c) w - \rho_m h_g \right]. \tag{D7}$$

References

Albert, R. A., R. J. Phillips, A. J. Dombard, and C. D. Brown (2000), A test of the validity of yield strength envelopes with an elastoviscoplastic finite element model, *Geophys. J. Int.*, *140*, 399–409.

Banerdt, W. B. (1986), Support of long-wavelength loads on Venus and implications for internal structure, *J. Geophys. Res.*, *91*, 403–419.

Bertka, C. M., and Y. Fei (1998), Density profile of an SNC model Martian interior and the moment-of-inertia factor of Mars, *Earth Planet. Sci. Lett.*, *157*, 79–88.

Breuer, D., T. Spohn, and U. Wullner (1993), Mantle differentiation and the crustal dichotomy of Mars, *Planet. Space Sci.*, *41*(4), 269–283.

Brückner, J., G. Dreibus, R. Rieder, and H. Wänke (2003), Refined data of Alpha Proton X-ray Spectrometer analyses of soils and rocks at the Mars Pathfinder site: Implications for surface chemistry, *J. Geophys. Res.*, *108*(E12), 8094, doi:10.1029/2003JE002060.

Britt, D. T., and G. J. Consolmagno (2003), Stony meteorite porosities and densities: A review of the data through 2001, *Meteorit. Planet. Sci.*, *38*, 1161–1180.

Clévédé, E., and P. Lognonné (2003), Normal modes of the Earth and Planets [software], in *Handbook on Earthquake and Engineering Seismology, Part B*, vol. 81B, edited by W. H. K. Lee, P. Jennings, and C. Kisslinger, chap. 85.16, Elsevier, New York.

Comer, R. P., S. C. Solomon, and J. W. Head (1985), Mars: Thickness of the lithosphere from the tectonic response to volcanic loads, *Rev. Geophys.*, *23*(1), 61–921.

Driscoll, J. R., and D. Healy (1994), Computing Fourier transforms and convolutions on the 2-sphere, *Adv. Appl. Math.*, *15*, 202–250.

Forsyth, D. W. (1985), Subsurface loading and estimates of flexural rigidity of continental lithosphere, *J. Geophys. Res.*, *90*(B14), 12,623–12,632.

Freed, A. M., H. J. Melosh, and S. C. Solomon (2001), Tectonics of mascon loading: Resolution of the strike-slip faulting paradox, *J. Geophys. Res.*, *106*, 20,603–20,620.

Frey, H. V., J. H. Roark, K. M. Shockey, E. L. Frey, and S. E. H. Sakimoto (2002), Ancient lowlands on Mars, *Geophys. Res. Lett.*, *29*(10), 1384, doi:10.1029/2001GL013832.

Hartmann, W. K., and G. Neukum (2001), Cratering chronology and the evolution of Mars, *Space Sci. Rev.*, *96*, 165–194.

Head, J. N., H. J. Melosh, and B. A. Ivanov (2002), Martian meteorite launch: High-speed ejecta from small craters, *Science*, *298*, 1752–1756.

Hoogenboom, T., S. E. Smrekar, F. S. Anderson, and G. Houseman (2004), Admittance survey of type 1 coronae on Venus, *J. Geophys. Res.*, *109*, E03002, doi:10.1029/2003JE002171.

Jolliff, B. L., J. J. Gillis, L. A. Haskin, R. L. Korotev, and M. A. Wieczorek (2000), Major lunar crustal terranes: Surface expressions and crust-mantle origins, *J. Geophys. Res.*, *105*, 4197–4216.

Jordan, T. H. (1979), Mineralogies, densities and seismic velocities of garnet lherzolites and their geophysical implications, in *The Mantle Sample: Inclusions in Kimberlites and Other Volcanics: Proceedings of the Second International Kimberlite Conference*, vol. 2, edited by F. R. Boyd and H. O. A. Meyer, pp. 1–14, AGU, Washington, D. C.

Kiefer, W. S. (2003), Melt in the Martian mantle: Shergottite formation and implications for present-day mantle convection on Mars, *Meteorit. Planet. Sci.*, *38*, 1815–1832.

Kraus, H. (1967), *Thin Elastic Shells: An Introduction to the Theoretical Foundations and the Analysis of Their Static and Dynamic Behavior*, 467 pp., John Wiley, Hoboken, N. J.

Lawrence, K. P., and R. J. Phillips (2003), Gravity/topography admittance inversion on Venus using niching genetic algorithms, *Geophys. Res. Lett.*, *30*(19), 1994, doi:10.1029/2003GL017515.

Lemoine, F. G., D. E. Smith, D. D. Rowlands, M. T. Zuber, G. A. Neumann, D. S. Chinn, and D. E. Pavlis (2001), An improved solution of the gravity field of Mars (GMM-2B) from Mars Global Surveyor, *J. Geophys. Res.*, *106*(E10), 23,359–23,376.

Lognonné, P., and B. Romanowicz (1990), Modeling of coupled normal modes of the Earth: The spectral method, *Geophys. J. Int.*, *102*, 365–395.

Lognonné, P., et al. (2000), The NetLander very broad band seismometer, *Planet. Space Sci.*, *48*, 1289–1302.

McGovern, P. J., S. C. Solomon, D. E. Smith, M. T. Zuber, M. Simons, M. A. Wieczorek, R. J. Phillips, G. A. Neumann, O. Aharonson, and J. W. Head (2002), Localized gravity/topography admittance and correlation spectra on Mars: Implications for regional and global evolution, *J. Geophys. Res.*, *107*(E12), 5136, doi:10.1029/2002JE001854.

McGovern, P. J., S. C. Solomon, D. E. Smith, M. T. Zuber, M. Simons, M. A. Wieczorek, R. J. Phillips, G. A. Neumann, O. Aharonson, and J. W. Head (2004), Correction to "Localized gravity/topography admittance and correlation spectra on Mars: Implications for regional and global evolution," *J. Geophys. Res.*, E07007, doi:10.1029/2004JE002286.

McKenzie, D., D. N. Barnett, and D.-N. Yuan (2002), The relationship between Martian gravity and topography, *Earth Planet. Sci. Lett.*, *195*, 1–16.

McNutt, M. K. (1984), Lithospheric flexure and thermal anomalies, *J. Geophys. Res.*, *89*, 11,180–11,194.

McSween, H. Y. (1985), SNC meteorites: Clues to Martian petrologic evolution?, *Rev. Geophys.*, *23*, 391–416.

Moore, J. G. (2001), Density of basalt core from Hilo drill hole, Hawaii, *J. Volcanol. Geotherm. Res.*, *112*, 221–230.

Neukum, G., et al. (2004), Recent and episodic volcanic and glacial activity on Mars revealed by the high resolution stereo camera, *Nature*, *432*, 971–979.

Neumann, G. A., M. T. Zuber, M. A. Wieczorek, P. J. McGovern, F. G. Lemoine, and D. E. Smith (2004), Crustal structure of Mars from gravity and topography, *J. Geophys. Res.*, *109*, E08002, doi:10.1029/2004JE002262.

Nimmo, F. (2002), Admittance estimates of mean crustal thickness and density at the Martian hemispheric dichotomy, *J. Geophys. Res.*, *107*(E11), 5117, doi:10.1029/2000JE001488.

Nyquist, L. E., D. D. Bogard, C.-Y. Shih, A. Greshake, D. Stöffler, and O. Eugster (2001), Ages and geologic histories of Martian meteorites, *Space Sci. Rev.*, *96*, 105–164.

Oxburgh, E. R., and E. M. Parmentier (1977), Compositional and density stratification in oceanic lithosphere—Causes and consequences, *J. Geol. Soc. London*, *133*, 343–355.

Pérez-Gussinyé, M., A. R. Lowry, A. B. Watts, and I. Velicogna (2004), On the recovery of effective elastic thickness using spectral methods: Examples from synthetic data and from the Fennoscandian Shield, *J. Geophys. Res.*, *109*, B10409, doi:10.1029/2003JB002788.

Phillips, R. J., et al. (2001), Ancient geodynamics and global-scale hydrology on Mars, *Science*, *291*, 2587–2591.

Phinney, R. A., and R. Burridge (1973), Representation of the elastic-gravitational excitation of a spherical Earth model by generalized spherical harmonics, *Geophys. J. R. Astron. Soc.*, *34*, 451–487.

Press, W. H., S. A. Teukolsky, W. T. Vetterling, and B. P. Flannery (1992), *Numerical recipes in FORTRAN: The Art of Scientific Computing*, 2nd ed., 654 pp., Cambridge Univ. Press, New York.

Simons, M., S. C. Solomon, and B. H. Hager (1997), Localization of gravity and topography: Constraints on the tectonics and mantle dynamics of Venus, *Geophys. J. Int.*, *131*, 24–44.

Smith, D. E., et al. (2001), Mars Orbiter Laser Altimeter MOLA: Experiment summary after the first year of global mapping of Mars, *J. Geophys. Res.*, *106*, 23,723–23,735.

Smrekar, S. E., R. Comstock, and F. S. Anderson (2003), A gravity survey of Type 2 coronae on Venus, *J. Geophys. Res.*, *108*(E8), 5090, doi:10.1029/2002JE001935.

Sneeuw, N. (1994), Global spherical harmonic analysis by least-squares and quadrature methods in historical perspective, *Geophys. J. Int.*, *118*, 707–716.

Sohl, F., and T. Spohn (1997), The interior structure of Mars: Implications from SNC meteorites, *J. Geophys. Res.*, *102*, 1613–1636.

Solomon, S. C., and J. W. Head (1990), Heterogeneities in the thickness of the elastic lithosphere of Mars: Constraints on heat flow and internal dynamics, *J. Geophys. Res.*, *95*, 11,073–11,083.

Tarantola, A. (1987), *Inverse Problem Theory: Methods for Data Fitting and Model Parameter Estimation*, 600 pp., Elsevier, New York.

Thurber, C. H., and M. N. Toksoz (1978), Martian lithospheric thickness from elastic flexure theory, *Geophys. Res. Lett.*, *5*, 977–980.

Turcotte, D. L., R. J. Willemann, W. F. Haxby, and J. Norberry (1981), Role of membrane stresses in the support of planetary topography, *J. Geophys. Res.*, *86*(B5), 3951–3959.

Wieczorek, M. A., and R. J. Phillips (1998), Potential anomalies on a sphere: Applications to the thickness of the lunar crust, *J. Geophys. Res.*, *103*, 1715–1724.

Wieczorek, M. A., and F. J. Simons (2005), Localized spectral analysis on the sphere, *Geophys. J. Int.*, *162*, 655–675, doi:10.1111/j.1365-246X.2005.02687.x.

Wieczorek, M. A., and M. T. Zuber (2004), Thickness of the Martian crust: Improved constraints from geoid-to-topography ratios, *J. Geophys. Res.*, *109*, E01009, doi:10.1029/2003JE002153.

Willemann, R. J., and D. L. Turcotte (1981), Support of topographic and other loads on the Moon and on the terrestrial planets, *Proc. Lunar Planet. Sci. Conf.*, *12B*, 837–851.

Zhong, S. (2002), Effects of lithosphere on the long-wavelength gravity anomalies and their implications for the formation of the Tharsis rise on Mars, *J. Geophys. Res.*, *107*(E7), 5054, doi:10.1029/2001JE001589.

Zhong, S., and M. T. Zuber (2000), Long-wavelength topographic relaxation for self-gravitating planets and implications for the time-dependent compensation of surface topography, *J. Geophys. Res.*, *105*(E2), 4153–4164.

Zuber, M. T., and D. E. Smith (1997), Mars without Tharsis, *J. Geophys. Res.*, *102*(E12), 28,673–28,686.

————————————

V. Belleguic, Institut für Planetenforschung, Deutsches Zentrum für Luft- und Raumfahrt (DLR), Rutherfordstrasse 2, D-12489 Berlin, Germany. (virginie.belleguic@dlr.de)

P. Lognonné and M. Wieczorek, Département de Géophysique Spatiale et Planétaire, Institut de Physique du Globe de Paris, 4 Avenue de Neptune, F-94107 Saint-Maur Cedex, France. (lognonne@ipgp.jussieu.fr; wieczor@ipgp.jussieu.fr)